

The DECADE cosmic shear project III: validation of analysis pipeline using spatially inhomogeneous data

D. Anbajagane (தயாஜாஜா)*^{1,2} C. Chang^{1,2} N. Chicoine^{1,3} L. F. Secco² C. Y. Tan^{4,2} P. S. Ferguson⁵ A. Drlica-Wagner^{6,1,2} K. Herron⁷ M. Adamow^{8,9} R. A. Gruendl^{8,9} M. R. Becker¹⁰ R. Teixeira^{1,11} Z. Zhang^{1,12,13} A. Alarcon¹⁴ D. Suson¹⁵ A. N. Alsina¹⁶ A. Amon¹⁷ F. Andrade-Oliveira¹⁸ J. Blazek¹⁹ H. Camacho²⁰ J. A. Carballo-Bello²¹ W. Cerny²² Y. Choi²³ C. Doux²⁴ M. Gatti² D. Gruen^{25,26} D. J. James^{27,28} E. Krause²⁹ N. Kuropatkin⁶ C. E. Martínez-Vázquez³⁰ P. Massana³¹ S. Mau^{32,12} J. McCullough³³ G. E. Medina^{34,35} B. Mutlu-Pakdil⁷ M. Navabi³⁶ N. E. D. Noël³⁶ A. B. Pace³⁷ A. Porredon³⁸ M. Raveri³⁹ A. H. Riley⁴⁰ J. D. Sakowska³⁶ S. Samuroff⁴¹ D. Sanchez-Cid^{18,42} D. J. Sand⁴³ L. Santana-Silva⁴⁴ M. Soares-Santos¹⁸ G. S. Stringfellow⁴⁵ C. To² A. K. Vivas⁴⁶ M. Yamamoto¹⁷ A. Zenteno⁴⁶ and J. Zuntz⁴⁷

¹ Department of Astronomy and Astrophysics, University of Chicago, Chicago, IL 60637, USA

² Kavli Institute for Cosmological Physics, University of Chicago, Chicago, IL 60637, USA

³ Department of Physics and Astronomy, University of Pittsburgh, 3941 O'Hara Street, Pittsburgh, PA 15260

⁴ Department of Physics, University of Chicago, Chicago, IL 60637, USA

⁵ DIRAC Institute, Department of Astronomy, University of Washington, 3910 15th Ave NE, Seattle, WA, 98195, USA

⁶ Fermi National Accelerator Laboratory, P. O. Box 500, Batavia, IL 60510, USA

⁷ Department of Physics and Astronomy, Dartmouth College, Hanover, NH 03755, USA

⁸ Center for Astrophysical Surveys, National Center for Supercomputing Applications, 1205 West Clark St., Urbana, IL 61801, USA

⁹ Department of Astronomy, University of Illinois at Urbana-Champaign, 1002 W. Green Street, Urbana, IL 61801, USA

¹⁰ Argonne National Laboratory, 9700 South Cass Avenue, Lemont, IL 60439, USA

¹¹ Department of Physics, Duke University Durham, NC 27708, USA

¹² Department of Physics, Stanford University, 382 Via Pueblo Mall, Stanford, CA 94305, USA

¹³ SLAC National Accelerator Laboratory, Menlo Park, CA 94025, USA

¹⁴ Institute of Space Sciences (ICE, CSIC), Campus UAB, Carrer de Can Magrans, s/n, 08193 Barcelona, Spain

¹⁵ Department of Chemistry and Physics, Purdue University Northwest 2200, 169th Ave, Hammond, IN 46323

¹⁶ Instituto de Física Gleb Wataghin, Universidade Estadual de Campinas, 13083-859, Campinas, SP, Brazil

¹⁷ Department of Astrophysical Sciences, Princeton University, Peyton Hall, Princeton, NJ 08544, USA

¹⁸ Physik-Institut, University of Zurich, Winterthurerstrasse 190, CH-8057 Zurich, Switzerland

¹⁹ Department of Physics, Northeastern University, Boston, MA 02115, USA

²⁰ Physics Department, Brookhaven National Laboratory, Upton, NY 11973

²¹ Instituto de Alta Investigación, Universidad de Tarapacá, Casilla 7D, Arica, Chile

²² Department of Astronomy, Yale University, New Haven, CT 06520, USA

²³ NSF National Optical-Infrared Astronomy Research Laboratory, 950 North Cherry Avenue, Tucson, AZ 85719, USA

²⁴ Université Grenoble Alpes, CNRS, LPSC-IN2P3, 38000 Grenoble, France

²⁵ University Observatory, Faculty of Physics, Ludwig-Maximilians-Universität, Scheinerstr. 1, 81679 Munich, Germany

²⁶ Excellence Cluster ORIGINS, Boltzmannstr. 2, 85748 Garching, Germany

²⁷ Applied Materials Inc., 35 Dory Road, Gloucester, MA 01930

²⁸ ASTRAVEO LLC, PO Box 1668, Gloucester, MA 01931

²⁹ Department of Astronomy/Steward Observatory, University of Arizona, Tucson, AZ 85721 USA

³⁰ International Gemini Observatory/NSF NOIRLab, 670 N. A'ohoku Place, Hilo, Hawai'i, 96720, USA

³¹ NSF's NOIRLab, Casilla 603, La Serena, Chile

³² Kavli Institute for Particle Astrophysics & Cosmology, P.O. Box 2450, Stanford University, Stanford, CA 94305, USA

³³ Department of Astrophysical Sciences, Peyton Hall, Princeton University, Princeton, NJ USA 08544

³⁴ David A. Dunlap Department of Astronomy & Astrophysics, University of Toronto, 50 St George Street, Toronto ON M5S 3H4, Canada

³⁵ *Dunlap Institute for Astronomy & Astrophysics, University of Toronto, 50 St George Street, Toronto, ON M5S 3H4, Canada*

³⁶ *Department of Physics, University of Surrey, Guildford GU2 7XH, UK*

³⁷ *Department of Astronomy, University of Virginia, 530 McCormick Road, Charlottesville, VA 22904, USA*

³⁸ *Centro de Investigaciones Energéticas, Medioambientales y Tecnológicas (CIEMAT), Madrid, Spain*

³⁹ *Department of Physics and INFN, University of Genova, Genova, Italy*

⁴⁰ *Institute for Computational Cosmology, Department of Physics, Durham University, South Road, Durham DH1 3LE, UK*

⁴¹ *Institut de Física d'Altes Energies, The Barcelona Institute of Science and Technology, Campus UAB, 08193 Bellaterra (Barcelona) Spain*

⁴² *Centro de Investigaciones Energéticas, Medioambientales y Tecnológicas (CIEMAT), Madrid, Spain*

⁴³ *Steward Observatory, University of Arizona, 933 North Cherry Avenue, Tucson, AZ 85721-0065, USA*

⁴⁴ *Centro Brasileiro de Pesquisas Físicas, Rua Dr. Xavier Sigaud 150, 22290-180 Rio de Janeiro, RJ, Brazil*

⁴⁵ *Center for Astrophysics and Space Astronomy, University of Colorado, 389 UCB, Boulder, CO 80309-0389, USA*

⁴⁶ *Cerro Tololo Inter-American Observatory/NSF NOIRLab, Casilla 603, La Serena, Chile*

⁴⁷ *Institute for Astronomy, University of Edinburgh, Edinburgh EH9 3HJ, UK*

Version February 26, 2025

ABSTRACT

We present the pipeline for the cosmic shear analysis of the Dark Energy Camera All Data Everywhere (DECADE) weak lensing dataset: a catalog consisting of 107 million galaxies observed by the Dark Energy Camera (DECam) in the northern Galactic cap. The catalog derives from a large number of disparate observing programs and is therefore more inhomogeneous across the sky compared to existing lensing surveys. First, we use simulated data-vectors to show the sensitivity of our constraints to different analysis choices in our inference pipeline, including sensitivity to residual systematics. Next we use simulations to validate our covariance modeling for inhomogeneous datasets. Finally, we show that our choices in the end-to-end cosmic shear pipeline are robust against inhomogeneities in the survey, by extracting relative shifts in the cosmology constraints across different subsets of the footprint/catalog and showing they are all consistent within 1σ to 2σ . This is done for forty-six subsets of the data and is carried out in a fully consistent manner: for each subset of the data, we re-derive the photometric redshift estimates, shear calibrations, survey transfer functions, the data vector, measurement covariance, and finally, the cosmological constraints. Our results show that existing analysis methods for weak lensing cosmology can be fairly resilient towards inhomogeneous datasets. This also motivates exploring a wider range of image data for pursuing such cosmological constraints.

1 INTRODUCTION

Over the past two decades, weak gravitational lensing (also referred to as weak lensing or cosmic shear) has emerged as a leading probe in constraining the cosmological parameters of our Universe (Asgari & Lin et al., 2021; Secco & Samuroff & Samuroff et al., 2022; Amon & Gruen et al., 2022; Dalal & Li et al., 2023). Weak lensing refers to the subtle bending of light from distant “source galaxies” due to the large-scale matter distribution between the source and the observer (Bartelmann & Schneider 2001). Thus, weak lensing, through its sensitivity to the matter distribution, probes the large-scale structure (LSS) of our Universe and any processes that impact this structure; including cosmological processes such as modified gravity (e.g., Schmidt 2008) and primordial signatures (e.g., Anbajagane et al. 2024c; Goldstein et al. 2024), as well as a wide variety of astrophysical processes (e.g., Chisari et al. 2018; Schneider et al. 2019; Aricò et al. 2021; Grandis et al. 2024; Bigwood et al. 2024). Weak lensing has many novel advantages in the landscape of cosmological probes, the primary of which is that it is an *unbiased* tracer of the density

field — unlike other tracers, such as galaxies — and does not require modeling or marginalizing over an associated bias parameter (Bartelmann & Schneider 2001). For these reasons, it is one of the leading probes of cosmology and has delivered some of our best constraints on cosmological parameters.

This paper is part of a series of works detailing the DECADE cosmic shear analysis. Anbajagane & Chang et al. 2025a (hereafter PAPER I) describes the shape measurement method, the derivation of the final cosmology sample, the robustness tests, and also the image simulation pipeline from which we quantify the shear calibration uncertainty of this sample. Anbajagane et al. (2025b, hereafter PAPER II) derives both the tomographic bins and calibrated redshift distributions for our cosmology sample, together with a series of validation tests. This work (PAPER III) describes the methodology and validation of the model, in addition to a series of survey inhomogeneity tests. Finally Anbajagane & Chang et al. 2025c (hereafter PAPER IV) shows our cosmic shear measurements and presents the corresponding constraints on cosmological models.

This work serves three, key purposes. First, to detail the

*dhayaa@uchicago.edu, chihway@kipf.uchicago.edu

modeling/methodology choices of the cosmic shear analysis, and the robustness of our results to said choices. Second, to build on the null-tests of [PAPER I](#) and show that our data vector (and cosmology) are not susceptible to contamination from systematic effects, such as correlated errors in the point-spread function (PSF) modeling. Finally, we test the impact of spatial inhomogeneity in the entire end-to-end pipeline used to extract the cosmology constraints. As highlighted in both [PAPER I](#) and [PAPER II](#), the DECADE dataset contains some unique characteristics relative to other WL datasets; particularly, the spatial inhomogeneity in the image data coming from this dataset’s origin as an amalgamation of many different public observing programs. We perform a suite of tests where we rerun the end-to-end pipeline for different subsets of our data — where each subset contains specific kinds of galaxies (red/blue, faint/bright etc.) or contains objects measured in regions of the sky with better/worse image quality (changes in seeing, airmass, interstellar extinction etc.) — and show that our cosmology constraints are robust across such subsets.

This paper is structured as follows. In Section 2, we briefly describe the DECADE shape catalog, and in Section 3, we present the cosmology model used in the DECADE cosmic shear project. In Section 4, we outline the different components required for parameter inference, including our analytic covariance matrix. In Section 5, we check the robustness of our constraints across modeling choice in simulated data vectors. Section 6 details our tests on the sensitivity of our parameter constraints to spatial inhomogeneity and to different selections of the source galaxy catalog. We conclude in Section 7.

2 THE DECADE DATASET

The DECADE dataset is a galaxy shape catalog of 107 million galaxies, spanning $5,412 \text{ deg}^2$ of the sky. The catalog is introduced in [PAPER I](#), alongside a suite of null-tests and shear calibrations made using image simulations of the survey data. The galaxy shears are estimated using the METACALIBRATION method ([Sheldon & Huff 2017](#)), with an approach designed to mimic that of DES Y3. In [PAPER II](#), we split the catalog into four tomographic bins and estimate the redshift distribution of the ensembles in each bin using the self-organizing maps photo-z (SOMPZ) method ([Buchs et al. 2019; Myles & Alarcon et al. 2021](#)), including cross-checking these estimates with alternative methods such as clustering redshifts ([Schneider et al. 2006; Newman 2008; Ménard et al. 2013; Davis et al. 2017; Gatti & Vielzeuf et al. 2018; Gatti & Giannini et al. 2022](#)).

The DECADE dataset is constructed from available community data (collected up to December 2022) from the Dark Energy Camera (DECam, [Flaugher et al. 2015](#)) within the footprint of interest to us; see Figure 2 in [PAPER I](#) for

the survey footprint, and also Section 2.1 in that work. The nature of this dataset — as an amalgamation of available archival data, rather than as a dedicated cosmological survey program — results in significant inhomogeneities in the survey observing conditions (such as depth). This, in turn, propagates into the observed object properties and therefore, the detection/selection functions of galaxy samples. While such inhomogeneities in observing conditions exist for other photometric galaxy surveys, such as DES, the variations are smaller relative to the DECADE inhomogeneities; see Figure 1. The latter part of this work (Section 6) explicitly shows the consistency in cosmology constraints when limiting our dataset to different regions of the sky with more/less spatial inhomogeneity in the chosen image quality.

In general, the constraining power of our catalog is fairly similar to that of DES Y3 ([PAPER I](#)). We have a source-galaxy number density that is $\approx 20\%$ lower than that of DES Y3 ($n_g = 4.6 \text{ arcmin}^{-2}$ compared to $n_g = 5.6 \text{ arcmin}^{-2}$); however, our footprint is $\approx 25\%$ larger (5412 deg^2 vs. 4143 deg^2). Thus, our lower number density is compensated by our larger area, and our shape catalog’s statistical precision is similar to that of DES Y3. Note, however, that our sample has slightly lower redshift ($\Delta\langle z \rangle \approx 0.02$), particularly in the highest tomographic bins ([PAPER II](#)).

3 MODELING

We use the two-point correlation function of galaxy shapes, $\xi_{\pm}(\theta)$ ([Bartelmann & Schneider 2001](#)), as our primary cosmological measurement. We have

$$\xi_{\pm}^{ij}(\theta) = \sum_{\ell} \frac{2\ell+1}{2\pi\ell^2(\ell+1)^2} \left[G_{\ell,2}^{+}(\cos\theta) \pm G_{\ell,2}^{-}(\cos\theta) \right] \times \left[C_{EE}^{ij}(\ell) \pm C_{BB}^{ij}(\ell) \right], \quad (1)$$

where the functions $G_{\ell}^{\pm}(x)$ are computed from Legendre polynomials $P_{\ell}(x)$ and averaged over angular bins ([Krause et al. 2021](#)). The i and j indices specify the two tomographic redshift bins from which the correlation function is calculated. Assuming the extended Limber approximation ([Limber 1953; Loverde & Afshordi 2008](#)) and in a spatially flat universe, the lensing power spectrum can be written as

$$C_{EE}^{ij}(\ell) = \int_0^{\chi_H} d\chi \frac{q^i(\chi)q^j(\chi)}{\chi^2} P_{\text{NL}}\left(\frac{\ell+1/2}{\chi}, \chi\right), \quad (2)$$

where χ is the radial comoving distance, χ_H is the distance to the horizon, P_{NL} is the nonlinear matter power spectrum, and $q(\chi)$ is the lensing efficiency defined via

$$q^i(\chi) = \frac{3}{2}\Omega_m \left(\frac{H_0}{c}\right)^2 \frac{\chi}{a(\chi)} \int_{\chi}^{\chi_H} d\chi' n_i(\chi') \frac{\chi' - \chi}{\chi'}, \quad (3)$$

where Ω_m is the matter density today, H_0 is the Hubble parameter today, a is the scale factor, and $n_i(\chi)$ is the redshift

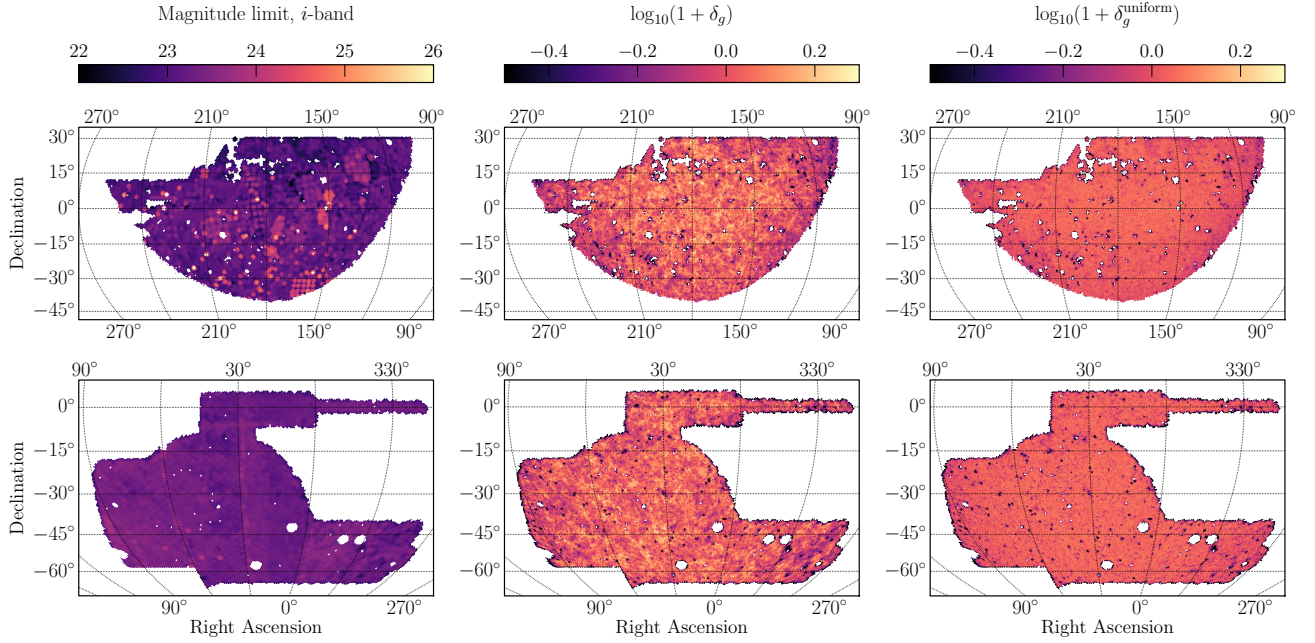


Figure 1. From left to right, we show the magnitude limit map in the i -band (estimated at $S/N = 10$ within a $2''$ aperture; see [PAPER I](#)), the overdensity in source galaxy number counts, δ_g , and the same after randomizing the galaxy positions within the survey mask. All maps are shown at $\text{NSIDE} = 1024$. The top row is for the DECADE data while the bottom is for DES Y3. While the DECADE magnitude limit map has significantly more structure relative to that of DES Y3, the DECADE source-galaxy sample has much less inhomogeneity as the DECADE and DES Y3 source-galaxy samples are defined with certain cuts (specifically $m_i < 23.5$) that make the variation in δ_g similar across the two surveys. The remaining large-scale variations, found towards the eastern/western edges of the footprint, are due to the closer proximity of the DECADE footprint to the galactic plane. The right-most panels show, as a simple reference, the number-density fluctuations for a sample with randomized positions. There are still some small fluctuations due to the mask structure on small scales; the mask is defined at $\text{NSIDE} = 4096$ ([PAPER I](#)).

distribution of the bin i . The term C_{BB}^{ij} will be non-zero due to the presence of intrinsic alignments (IA);¹ see Section 3.2 for discussions on our IA model.

Following the model described above, we consider several additional elements that are briefly described below. We note that we have largely followed the modeling framework used in the DES Year 3 (Y3) analysis ([Krause et al. 2021](#)), which is implemented in the public version of the CosmoSIS software ([Zuntz et al. 2015](#)). We will explicitly identify cases where our model deviates from that of DES Y3.

3.1 Nonlinear power spectrum

On small scales, the nonlinearity of structure formation as induced by gravity necessitates a modification of the matter power spectrum from the linear model, where the latter is typically calculated via a Boltzmann solver such as CAMB ([Lewis et al. 2000](#)) or CLASS ([Lesgourgues 2011](#)). Over the years, as the resolution and fidelity of N-body

¹ In practice, lensing also generates a C_{BB}^{ij} term but its amplitude is orders of magnitude lower than the C_{EE}^{ij} term and is therefore ignored (e.g., [Krause & Hirata 2010](#)).

simulations have improved and so has the prescription for the nonlinear power spectrum. In the DES Y1 and Y3 cosmic shear analysis, HALOFIT ([Takahashi et al. 2012](#)) was used and validated as the default nonlinear power spectrum. However, the study and joint-analysis between DES and the Kilo Degree Survey (KiDS) in [DES and KiDS Collaborations et al. \(2023\)](#) show that the updated version of HMCODE (HMCODE2020, [Mead et al. 2020, 2021](#)) provides a more accurate description when tested against the Euclid emulator ([Euclid Collaboration: Knabenhans et al. 2019](#)). At $k < 10h\text{Mpc}^{-1}$, HMCODE2020 has an accuracy of $< 2.5\%$. As a result, we adopt HMCODE2020 as the fiducial model for our nonlinear power spectrum. Note that for the constraining power of the DECADE data, we do not expect any significant differences in constraints when switching between the HALOFIT or HMCODE2020 models. We explicitly test this modeling choice in our simulated chains below, and also check it directly on the data in [PAPER IV](#).

The structure on these small scales is also impacted by the non-gravitational processes of baryons; most prominently, the ejection of gas from the halo due to feedback processes ([Chisari et al. 2018](#)). Hydrodynamical simulations (see [Vogelsberger et al. 2020](#), for a review), which model

these effects through approximate “subgrid” prescriptions, generate a variety of predictions for the properties of halos in simulations (*e.g.*, Anbajagane et al. 2020; Lim et al. 2021; Lee et al. 2022; Stiskalek et al. 2022; Anbajagane et al. 2022a,b; Shao et al. 2023; Shao & Anbajagane 2024; Gebhardt et al. 2023) and therefore also for the changes in the nonlinear matter power spectrum (*e.g.*, Chisari et al. 2018; Amon & Efstathiou 2022). These variations have been captured through phenomenological, halo-based models such as “Baryonification” (Schneider & Teyssier 2015; Schneider et al. 2019; Aricò et al. 2021; Anbajagane et al. 2024a) and the HMCode2020 model discussed above.

The HMCode2020 model includes a T_{AGN} parameter that quantifies the baryonic contribution to the nonlinear matter power spectrum, and this parameter was varied in the joint-analysis of DES and KiDS (DES and KiDS Collaborations et al. 2023). In this work, our fiducial analysis does not use any of these techniques and follows DES Y3 (Secco & Samuroff et al. 2022; Amon et al. 2022): we remove any scales where the baryonic effects are significant and analyze the remaining scales with a model that does not account for baryons. The identification of scales to be removed is done using the procedure described in Section 4.1. However, we also perform a variant analysis in PAPER IV that uses all measurements (*i.e.*, does not perform any scale cuts) and instead varies the T_{AGN} parameter to include the effects of baryons.

3.2 Intrinsic alignment (IA)

While cosmic shear manifests in the spatial correlations of galaxy shapes, these shapes can also be spatially correlated in the absence of lensing due to the gravitational environment, or tidal fields, that the galaxies form within (see, *e.g.*, the review Troxel & Ishak 2015, and references therein). This effect is referred to as intrinsic alignment.

The cosmic shear analysis of DES Y1 uses the nonlinear alignment model (NLA, Hirata & Seljak 2004; Bridle & King 2007; Joachimi et al. 2011). This model assumes that the IA power spectrum is proportional to the nonlinear matter power spectrum in a scale-independent way, through a function, $F[\chi(z)]$, given by

$$F[\chi(z)] = A_{\text{IA}} C_1 \rho_{\text{crit}} \frac{\Omega_m}{D_+(z)} \left(\frac{1+z}{1+z_0} \right)^\eta, \quad (4)$$

where A_{IA} is the amplitude parameter, $C_1 = 5 \times 10^{-14} h^{-2} M_\odot^{-1} \text{Mpc}^3$, ρ_{crit} is the critical density at $z = 0$, and $D_+(z)$ is the linear growth factor normalized to unity at $z = 0$ (Bridle & King 2007).

The DES Y3 analysis uses the more general, Tidal Alignment and Tidal Torquing model (TATT, Blazek et al.

2019). The TATT model extends from the NLA model and includes a tidal torquing alignment mechanism. It allows for five free nuisance parameters: a tidal alignment amplitude (a_1) with redshift evolution (η_1); a tidal torquing amplitude (a_2) with redshift evolution (η_2); and a linear bias amplitude (b_{TA}). The TATT model reduces to the NLA model when setting $a_1 = A_{\text{IA}}$, $\eta = \eta_1$, and $a_2 = \eta_2 = b_{\text{TA}} = 0$. Different analyses of DES Y3 have used either TATT (Secco & Samuroff et al. 2022; Amon et al. 2022; Samuroff et al. 2023) or NLA (DES and KiDS Collaborations et al. 2023) as their fiducial choice. For the DECADE cosmic shear analysis, given the unique nature of our dataset, we will adopt the more conservative TATT model as our fiducial choice but test the change in our results if we revert to the simpler NLA models.²

3.3 Shear and redshift calibration uncertainties

The two main sources of systematic uncertainties on our measurements are those associated with the shear estimate and the redshift distribution estimate. We follow the implementation from DES Y3 (Secco & Samuroff et al. 2022; Amon et al. 2022) — which is consistent with those of numerous other works (*e.g.*, Asgari et al. 2021; Dalal et al. 2023) — in the modeling of these uncertainties.

For any shear measurement algorithm, a “calibration” step is needed for the measured shear. This calibration is obtained either from simulations or the data itself, and there is an associated uncertainty with the calibration estimate. In the weak lensing regime, the residual impact of any biases on the measured shear, γ_{obs} , is modeled with both multiplicative m_i and additive components c_i (Huterer et al. 2006; Heymans et al. 2006; Bridle & King 2007), that scale the true shear γ_{true} as

$$\gamma_{\text{obs}} = \gamma_{\text{true}}(1 + m_i) + c_i, \quad (5)$$

where m_i and c_i are constants corresponding to the i^{th} redshift bin. The additive, residual bias often has a sufficiently small amplitude to not be relevant. Furthermore, the shear measurements of our catalog are mean-subtracted (PAPER I) following the approach in other works (*e.g.*, Zuntz & Sheldon et al. 2018; Gatti & Sheldon et al. 2021; Yamamoto & Becker et al. 2025). This naturally corrects for such additive biases in the data. The multiplicative residual bias, however, scales the amplitude of ξ_\pm and thus propagates directly to key cosmological constraints. As a result, accurate estimates of m_i are a necessity. We have made such estimates for our shear catalog using a suite of simulated images of the DECADE survey, as described in detail in PAPER I. The simulations inform priors for m_i which are listed in Table 1.

² Given TATT has more free parameters, there is now a higher chance for the constraints to explore unexpected parts of parameter space, due to the model having more freedom than can be constrained with the data. For this reason, it is often useful to check our results using NLA as well.

For the redshift distribution, we also follow DES Y3 using a shift in the mean redshift, Δz_i , per bin that then shifts the measured $n(z)$ for each bin i as

$$n_i(z) = n_{\text{fid},i}(z - \Delta z_i). \quad (6)$$

This parametrization keeps the shape of the $n(z)$ unchanged. While one could explore more complicated parametrizations of the $n(z)$ uncertainties, the above model is sufficient for the statistical power of our data (which is similar to DES Y3). In PAPER II, we derived the priors on Δz_i using the self-organizing map photo-z (SOMPZ) method while accounting for a variety of uncertainty contributions including cosmic variance, shot noise, redshift bias, and photometric zeropoint uncertainties. In the Appendix A of PAPER II, we also derived estimates of the $n(z)$ from combining SOMPZ with an independent estimate, clustering redshifts (WZ). The latter method includes information from the spatial clustering between our shear sample and spectroscopic sources. The former, SOMPZ-only method is our fiducial choice, while we use the latter SOMPZ plus WZ method as a cross-check. The resulting priors on Δz_i from the fiducial setting are listed in Table 1.

4 PARAMETER INFERENCE

We now describe the components, in addition to the model described in Section 3, that are required for the final parameter inference.

4.1 Scale cuts

As we discussed in Section 3.1, baryons can influence the matter power spectrum on a wide range of scales, presenting a significant source of uncertainty. For example, feedback processes from AGN and supernovae can heat environments and suppress matter clustering, while metal enrichment may offer cooling channels that increase small-scale clustering (e.g., Chisari et al. 2018; Schneider et al. 2019). To reduce the impact of these baryonic imprints, we follow Secco & Samuroff et al. (2022) and Amon et al. (2022) in removing shear measurements whose signal can have a significant contribution from baryon evolution. In particular, we use a simulated data vector derived with the matter-power spectrum measured in the “AGN” model of the Overwhelmingly Large Simulations (OWLS, Schaye et al. 2010, see their Table 2) as a representative example for the baryonic imprints/contamination. The current estimates of the power-spectrum suppression from data are consistent with this OWLS model Bigwood et al. (e.g., 2024, see their Figure 1 and 4).

Our scale cuts are set by requiring the contaminated and uncontaminated data vectors to differ by $\Delta\chi^2 < 0.3$. This roughly follows the scale-cuts procedure used in DES Y3. In

this work, we derive the scale cuts with the following steps, starting from the unmasked data vector:

- Compute $(\Delta\chi^2)_i = (D_{\text{contam}}^i - D_{\text{uncontam}}^i)^2 / \sigma_i^2$ on each data point i individually, where σ_i is the uncertainty associated with data point i ,
- Find the measurement at the smallest scale in each bin. We have 10 combinations of tomographic bin pairs and two correlation functions, ξ_+ and ξ_- , resulting in 20 points selected for potential masking,
- Of the 20 selected points from the previous step, we find the data point with the highest $\Delta\chi^2$ and remove it. We repeat this iteratively until the $\Delta\chi^2$ between the contaminated and uncontaminated data vectors, after masking/scale cuts, is ≤ 0.3 .

The ξ_- shear measurements are more heavily affected by baryon contamination and thus require more impactful scale cuts. In practice we remove a similar number of points as the fiducial DES Y3 scale cuts (Secco & Samuroff et al. 2022; Amon et al. 2022); our final data vector has 220 data points whereas the fiducial data vector from DES Y3 has 222 data points.

As a final step, we analyze a data vector *with* baryon imprints while using our fiducial model, which includes scale cuts but no baryon modelling. We then check that the cosmological constraints in the $\Omega_m - S_8$ plane are shifted by less than 0.3σ . This result is detailed further below in Section 5.1. Note that there are other valid approaches for determining which measurements to discard from the full data vector. The only clear requirement is that after scale cuts are applied, the posterior constraint from the data vector must shift by less than 0.3σ when the data vector is contaminated with baryonic imprints. Our method above is one such approach and results in scale cuts that are similar to those of DES Y3, as mentioned above.

4.2 Covariance matrix

The parameter inference described in Section 4.3 below requires estimating the covariance of our measurements. In this work, we generate an analytical covariance using the CosmoCov package (Krause & Eifler 2017; Fang et al. 2020a,b). There are many advantages of using an analytical covariance matrix over one estimated from simulations or from the data itself. A key advantage is that such a covariance matrix does not contain numerical noise and can therefore be robustly inverted to obtain the likelihood. This approach of analytically modeling the covariance is also adopted in the DES Y3 analyses (Friedrich et al. 2021).

CosmoCov uses a two-dimensional FFTLog method to efficiently calculate the real-space, non-Gaussian covariance matrix for galaxy weak lensing (as well as other probes not considered in this work). This covariance can be decomposed as,

$$\mathbf{C} = \mathbf{C}_G + \mathbf{C}_{\text{SSC}} + \mathbf{C}_{\text{cNG}}, \quad (7)$$

where \mathbf{C}_G is the standard Gaussian covariance matrix, and the two non-Gaussian contributions include a connected four-point correlation (\mathbf{C}_{cNG}) that accounts for the presence of nonlinear structure (Wagner et al. 2015; Barreira & Schmidt 2017a,b) and then a super sample contribution (\mathbf{C}_{SSC}) which accounts for cross-correlations between different small-scale modes induced by modes larger than the survey footprint (e.g., Barreira et al. 2018). The non-Gaussian contributions are subdominant for the diagonal elements of \mathbf{C} but are dominant in the off-diagonal terms as their primary effect is in coupling together different modes/scales.

Certain terms in the final covariance can have some sensitivity to the geometry of the survey mask, and some can also have sensitivity to the distribution of galaxies within that mask. We first recast Equation (7) by splitting the covariance into the following terms

$$\mathbf{C} = \mathbf{C}_{\text{SN}} + \mathbf{C}_{\text{mix}} + \mathbf{C}_{\text{CV/SSC/cNG}}, \quad (8)$$

where \mathbf{C}_{SN} is the shape-noise term, $\mathbf{C}_{\text{CV/SSC/cNG}}$ is the sum of the cosmological terms (i.e., the sole term in the covariance when shape noise is negligible), and \mathbf{C}_{mix} is the mixed term which contains one power each of the cosmological signal and the noise field. In CosmoCov, the terms \mathbf{C}_{SN} and \mathbf{C}_{SSC} (that is, just the super-sample covariance term in $\mathbf{C}_{\text{CV/SSC/cNG}}$) include the effects of the survey mask, while the rest ignore it. Friedrich et al. (2021) explicitly show that the impact of the mask on the mixed covariance term, as well as the cosmic variance and connected four-point terms, changes the posterior width by less than 1% (see their Figure 2). The DECADE survey footprint has a similarly regular geometry relative to that of the DES footprint,³ and we therefore follow Friedrich et al. (2021) in assuming the mask can be ignored in the mixed term.

The contribution of the shape noise term is sensitive to the inhomogeneity in the *source-galaxy number density*. Note that this is *not* the inhomogeneity in the image quality/depth. Figure 1 illustrates the relevance of this distinction. The left panels show the magnitude limit maps from DECADE and from DES Y3, both generated using the DECASU software.⁴ There is a clear visual difference in the homogeneity of these maps. However, this does not directly translate into the middle column, which shows the number density map, n_{gal} , of the

shape catalog. The catalogs in both DES Y3 and DECADE are defined with a cut $m_i < 23.5$, which is around the median depth of the DECADE survey. This means the long tail to high magnitude limits (Figure 5 below, or also Figure 1 in PAPER I) is alleviated through this cut. Note that this cut was placed in Y3, and is replicated in DECADE, in order to improve the accuracy of our photometric redshift estimates (Myles & Alarcon et al. 2021). The middle column of Figure 1 shows that the distribution of n_{gal} is in fact similar across DECADE and DES Y3. In summary, while the DECADE survey's observing conditions are more inhomogeneous than DES Y3, the number density of the resulting source-galaxy catalog is similarly homogeneous to that of DES Y3.

Given our survey mask has a regular geometry and similar small-scale feature compared to DES Y3, we rely on the findings on Friedrich et al. (2021) and do not re-validate the \mathbf{C}_{mix} and $\mathbf{C}_{\text{CV/SSC/cNG}}$ terms in Equation (7). In this context, we only need to check the impact of inhomogeneity on the shape noise-related terms. As a reminder, the covariance model of Friedrich et al. (2021) included the survey mask in \mathbf{C}_{SN} term, using the method of Troxel et al. (2018), and ignored it in the mixed term (as it contributed only 1% to the posterior scatter, as mentioned above). The variations in galaxy number density within the mask was not included when accounting for the mask. In Appendix C, we confirm that these variations have a minimal impact in the covariance estimate for the DECADE dataset and can therefore be ignored, as was done in DES Y3.

4.3 Likelihood and sampling

We fit the model above to the cosmic shear measurements of ξ_{\pm} using a Markov Chain Monte Carlo (MCMC) approach. We assume a Gaussian likelihood L , with

$$\ln L(\xi_{\pm,d}|\mathbf{p}) = -\frac{1}{2} \left(\xi_{\pm,d} - \xi_{\pm,m}(\mathbf{p}) \right) \mathbf{C}^{-1} \left(\xi_{\pm,d} - \xi_{\pm,m}(\mathbf{p}) \right), \quad (9)$$

where $\xi_{\pm,d}$ and $\xi_{\pm,m}$ are the ξ_{\pm} data vector measured in the data and that predicted by the theoretical model of Equation 1, respectively; \mathbf{C}^{-1} is the inverse covariance described in Section 4.2; \mathbf{p} is a vector of cosmological model parameters and nuisance parameters listed in Table 1. The Bayesian posterior is proportional to the product of the likelihood L and the prior P ,

$$P(\mathbf{p}|\xi_{\pm,d}) \propto L(\xi_{\pm,d}|\mathbf{p})P(\mathbf{p}). \quad (10)$$

In Table 1 we list the priors as well as fiducial values of all the model parameters.

We perform the parameter inference using the CosmoSIS package (Zuntz et al. 2015). In particular, we use the Nautilus sampler (Lange 2023) for most of our tests, and the Polychord sampler (Handley et al. 2015) for the final

³ The structure of our small-scale mask features is the same as that of DES given we use a similar masking procedure that removes circular regions around bright sources (PAPER I).

⁴ <https://github.com/erykoff/decasu>

Parameter	Fiducial	Prior
Cosmology		
Ω_m	0.27	$\mathcal{U}(0.1, 0.9)$
Ω_b	0.048	$\mathcal{U}(0.03, 0.07)$
h	0.69	$\mathcal{U}(0.55, 0.91)$
$A_s \times 10^9$	–	$\mathcal{U}(0.5, 5)$
σ_8	0.846	–
n_s	0.97	$\mathcal{U}(0.87, 1.07)$
$\Omega_s h^2$	0.00083	$\mathcal{U}(0.0006, 0.00644)$
Intrinsic Alignments		
a_1	0.19	$\mathcal{U}(-4, 4)$
a_2	-0.47	$\mathcal{U}(-4, 4)$
η_1	-2.6	$\mathcal{U}(-4, 4)$
η_2	3.38	$\mathcal{U}(-4, 4)$
b_{ta}	0.0066	$\mathcal{U}(0, 2)$
Redshift calibration		
Δz_1	0.0	$\mathcal{N}(0, 0.0163)$
Δz_2	0.0	$\mathcal{N}(0, 0.0139)$
Δz_3	0.0	$\mathcal{N}(0, 0.0101)$
Δz_4	0.0	$\mathcal{N}(0, 0.0117)$
Shear calibration		
m_1	0.0	$\mathcal{N}(-0.00923, 0.00296)$
m_2	0.0	$\mathcal{N}(-0.01895, 0.00421)$
m_3	0.0	$\mathcal{N}(-0.04004, 0.00428)$
m_4	0.0	$\mathcal{N}(-0.03733, 0.00462)$

Table 1. Cosmology and nuisance parameters in the baseline Λ CDM model. Uniform distributions in the range $[a, b]$ are denoted $\mathcal{U}(a, b)$ and Gaussian distributions with mean μ and standard deviation σ are denoted $\mathcal{N}(\mu, \sigma)$. The column “Fiducial” refers to the parameters used for generating the synthetic data vector in all the simulated likelihood tests.

Sampler	Parameter	Value
Polychord	fast_fraction	0.1
	live_points	500
	num_repeats	60
	tolerance	0.01
	boost_posteriors	10.0
Nautilus	n_live	1500
	discard_exploration	True
Multinest	live_points	500
	efficiency	0.3
	tolerance	0.1
	constant_efficiency	False

Table 2. Parameters used in the different samplers tested in Section 5.4. Nautilus is the primary sampler used in this project. polychord, which is the default sampler in DES, is used to validate our results from Nautilus.

cosmological constraints that are shown in PAPER IV. The exact parameters we use for the two samplers are listed in Table 2.

5 VALIDATION OF FIDUCIAL MODEL

In this section we validate our model — specifically, testing that it is sufficient for obtaining unbiased constraints — by generating simulated data vectors and analyzing them using the pipeline. We generate a fiducial data vector using the parameters in the “Fiducial” column in Table 1. In particular, the IA parameters have fiducial values taken to be the best-fit parameters from the DES Y3 $3 \times 2\text{pt}^5$ results (DES Collaboration 2022). The cosmological parameters were first chosen to be generic ($\Omega_m = 0.3$, $\sigma_8 = 0.8$) in the initial testing, but after unblinding of our final cosmology constraints (see PAPER IV) we updated the values to more closely match said constraints. Regardless, the tests in this paper are quite insensitive to the assumed cosmology and to the relatively small shifts we applied pre/post-unblinding.

In Figure 2, we show the resulting cosmological constraint of our fiducial model in the plane spanned by Ω_m , σ_8 , and $S_8 \equiv \sigma_8 \sqrt{\Omega_m/0.3}$. The input cosmology is indicated by the cross-hair and shows our pipeline recovers the input parameters. This is a simple check, but can be non-trivial due to the impact of parameter projection effects (also called “prior volume” effects) in the high-dimensional parameter space as in such cases the marginalized 1D constraints are not guaranteed to be centered at/around the truth. Of the parameters shown in Figure 2, we focus on the derived parameter S_8 , which has been widely adopted in the lensing community since it approximates the most constraining direction in the σ_8 - Ω_m plane (Jain & Seljak 1997). Our simulated analysis shows $S_8 = 0.801^{+0.024}_{-0.024}$.

We also overlay the DES Y3 constraints (Secco & Samuroff et al. 2022; Amon et al. 2022) for comparison: $S_8 = 0.759^{+0.025}_{-0.023}$ and $S_8 = 0.772^{+0.018}_{-0.017}$ for the “Fiducial” and “Optimal” cases, respectively. The “Optimal” case cuts fewer scales from the final analysis. Our focus is the relative size of the contours, and not the relative locations (as we are doing a simulated analysis for the DECADE dataset and have complete freedom in the location of the resulting contour), so we shift the DES posteriors to be centered on the input cosmology of the simulated data vector. The figure shows the DECADE constraints are expected to be similar to the DES Y3 “Fiducial” constraints, and broader than the DES Y3 “Optimal” constraints. Our scale cuts match the former setup. We also note that all DES constraints shown here include information from shear ratios (Sánchez & Prat et al. 2022). We perform a more detailed comparison of the DECADE and DES Y3 constraints in PAPER IV and find the DECADE result slightly outperform the DES Y3 “Fiducial” result once all analysis choices are matched.

⁵ The 3×2 nomenclature of DES refers to the combination of two-point correlation functions of three probes: galaxy clustering, galaxy galaxy-lensing, and cosmic shear.

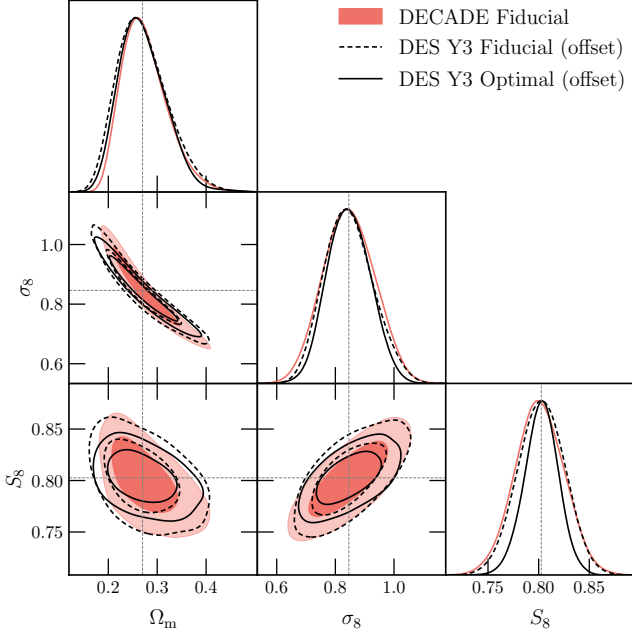


Figure 2. Forecasted constraints on Ω_m , σ_8 and S_8 using a simulated data vector corresponding to the DECADE dataset. The cross-hair indicates the input cosmology, showing that our pipeline adequately recovers the input values. The DES Y3 constraints from [Secco & Samuroff et al. \(2022\)](#) and [Amon et al. \(2022\)](#) are overlaid for comparison. To enhance comparisons of constraining power, we shift the DES posteriors to be centered on the simulated data vector’s input cosmology. Both the fiducial and the optimal constraints from DES include information from shear ratios ([Sánchez & Prat et al. 2022](#)), resulting in tighter constraining power and slightly different degeneracy directions.

In the following subsections we perform a number of stress-tests on the model. We summarize all the tests in Figure 3, where we show the marginal constraints in S_8 , Ω_m and σ_8 , and compare it with the fiducial constraints in Figure 2. First, Section 5.1 confirms that our fiducial scale cuts (derived in Section 4.1) alleviate biases from baryonic imprints in the data vector. Next, Section 5.2 discusses shifts in constraints when assuming different models for the nonlinear matter power spectrum and the IA. In Section 5.3 we examine the sensitivity of our constraints to the priors on the nuisance parameters, and in Section 5.4, the sensitivity of the constraints to the choice of sampling methods.

In Appendix A, we also verify that (1) the contamination from correlations of the point-spread function has negligible impact on our cosmology constraints, and; (2) there is no statistically significant detection of B -modes in all auto- and cross-correlations of our data vector. Both tests complement those found in [PAPER I](#).

5.1 Robustness to small-scale modeling / baryons

As discussed in Section 4.1, we remove measurements from small-scale correlations during our inference as there are large uncertainties in the matter power spectrum model on such scales, primarily due to the effects of baryons ([Chisari et al. 2018](#)). In Figure 3, we show constraints with and without scale cuts, for both the fiducial data vector (line 1 and 3) and also one contaminated by baryon effects (line 2 and 4). The contaminated data-vector is the same one used to determine the scale cuts described in Section 4.1. The case “without scale cuts” uses all measured data points from $2.5' < \theta < 250'$ for the data-vector in question.

We first compare line 1 and 3. Without baryonic contaminations, we see that both constraints are centered on the input values of the cosmological parameters, and the scale cuts degrade the constraints by a factor of ≈ 2 . This highlights the significant cosmological information in the scales that we currently remove due to baryonic effects. Next, we compare the pairs of line 3 and 4, and then line 1 and 2. If we do not use scale cuts, the contamination from baryonic effects shifts the extracted constraints. We evaluate the shift in the Ω_m - S_8 plane to be 0.67σ . Once we apply the scale cuts, the shifts reduce to 0.01σ , which is within our criteria of 0.3σ . Note that the shift moves in the direction that decreases S_8 , which is expected as baryonic feedback suppresses the matter power spectrum on the small scales relevant for weak lensing ([Chisari et al. 2018](#); [Amon & Efstathiou 2022](#)).

5.2 Robustness to nonlinear power spectrum and IA models

We have made certain choices in the modeling pipeline based on our best, current knowledge (which is informed by the latest cosmic shear analyses) on the validity/accuracy of each model. In particular, the nonlinear power spectrum and IA model are chosen based on arguments detailed in Section 3. In this section we check the shift in S_8 constraints if under alternative choices for these models. Note that in all cases, the changes are made only to the analysis pipeline; the simulated data vector is still generated using our fiducial setup.

Line 5 in Figure 3 shows the S_8 constraints when using HALOFIT as our model for the nonlinear matter power spectrum. Using HALOFIT to analyze a HMCODE-generated data vector shifts the S_8 constraint to a slightly lower value, which is consistent with what is seen in *e.g.*, [Secco & Samuroff et al. \(2022\)](#), and is because at fixed cosmology, the HALOFIT model predicts slightly more power on nonlinear scales relative to HMCODE ([Mead et al. 2016, 2020](#)). Moving onto IA model choices, line 7 in Figure 3 shows that the use of NLA (with two free parameters) tightens the cosmological constraints slightly ($\approx 8\%$) relative to TATT, which has five free parameters. TATT

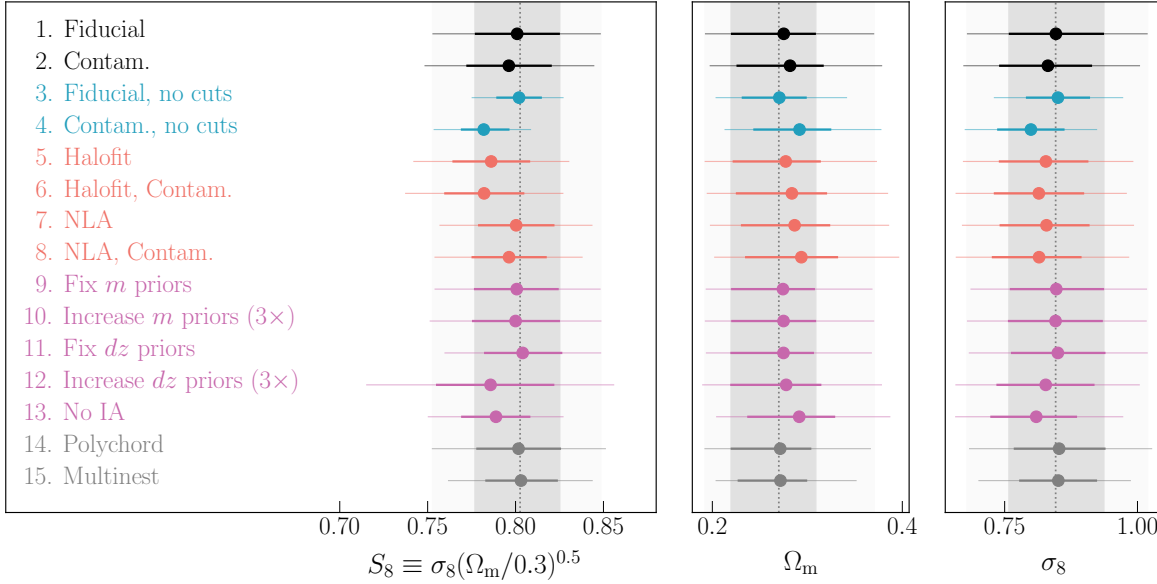


Figure 3. Constraints on S_8 , Ω_m and σ_8 from simulated data vectors, under different analysis choices. This series of tests (detailed in Section 5) ensures that the modeling choice we adopted for the data is robust, including the mitigation of small-scale baryonic effects, the assumptions of the nonlinear power spectrum and intrinsic alignment, the priors on the nuisance parameters, and the choice of sampling approaches in the inference process. In this plot, as well as later Figures 4 and 6, the constraints shown are the marginalized mean, 1σ and 2σ uncertainties. The vertical shaded region correspond to the 1σ (dark) and 2σ (light) intervals of the fiducial case. Here, we also show the true input value to the simulated data vectors with the vertical dotted line. Note that line 1 (“Fiducial”) corresponds to the marginal constraints shown in Figure 2.

is a more general model for intrinsic alignments and includes three additional parameters (see Table 1).

We also check that our scale cuts, determined in Section 5.1, reduce baryon-driven biases in S_8 even for the alternative models. We re-estimate the parameter shifts from baryon contamination using HALOFIT as our nonlinear matter power spectrum model and find a shift of 0.08σ (comparing line 5 and 6 in Figure 3). Repeating this after changing the IA model to NLA resulted in a shift of only 0.05σ (comparing line 7 and 8 in Figure 3).

5.3 Impact of priors on nuisance parameters

We next check the impact of the different nuisance parameter marginalization on the final constraining power. Starting from the fiducial analysis setup, we either fix or broaden priors for the shear calibration m and the mean redshift calibration Δz . We also run a variant where we fix the IA parameters. Line 9-13 of Figure 3 shows the different constraints from changing the priors on these nuisance parameters. The shear calibration uncertainties (m priors) are subdominant, as narrowing/widening the parameter priors has negligible impact on the final constraints (line 9 and 10). The parameters associated with the redshift uncertainty show some small effect as fixing their values reduces the uncertainty in S_8 by $\approx 8\%$ (line 11) and widening the prior by three times increases the uncertainty in S_8 by $\approx 20\%$ (line

12). Finally, fixing all IA parameters improves the constraints ($\approx 33\%$, line 13) relative to our fiducial case. These results indicate after our scale cuts are applied, our constraining power is not limited by systematic uncertainties from our shear and redshift calibrations, *i.e.*, improving our precision on these systematic parameters will not significantly reduce the uncertainties on S_8 . We *are*, however, limited by our uncertainties in the IA parameters. This is also explored in more detail in the data analysis of PAPER IV.

5.4 Robustness to sampling choices and noise

As discussed in Section 4.3, all cosmology results for our tests (including those found below and those in PAPER I) are obtained using the Nautilus (Lange 2023) sampler, whereas our main cosmology results will be extracted using the Polychord sampler (Handley et al. 2015) run on the high accuracy setting (Table 2). We show in line 1 and 14 of Figure 3 that under the fiducial settings, the results from Nautilus and Polychord are very consistent with each other both in the mean and the width of the posterior on S_8 . Therefore, we use Nautilus to obtain the rest of the constraints presented in this work and all constraints in PAPER IV. We also show in line 15 the same analysis run with the Multinest sampler, which show slightly underestimated error bars (by about 7% in S_8). This has been pointed out in previous work (Lemos & Weaverdyck et al. 2023) and we confirm that result here.

6 IMPACT OF SPATIAL INHOMOGENEITIES

As discussed previously, the DECADE cosmic shear catalog is constructed using image data from a wide variety of community-led campaigns, which in turn results in a variety of observing conditions and image quality. This is in contrast to other dedicated lensing surveys — such as DES, KiDS, and Subaru Hyper Suprime Cam (HSC, Miyazaki et al. 2018) — where homogeneity in image quality and depth is a target of the survey observing strategy.

We reiterate a subtlety discussed above in Section 4.2: the impact of survey inhomogeneity on source galaxy number counts, n_{gal} , is largely alleviated through our sample selection (a cut of $m_i < 23.5$), and so the remaining, predominant impact of inhomogeneous image quality is on the measured galaxy properties. Figure 1 illustrates this point. This *does not* mean the DECADE survey is “as homogeneous” as DES Y3. The observing conditions of the survey — which we will describe below in Section 6.2 — will impact the distribution of measured galaxy properties in a spatially dependent manner. This can still impact the measurements and therefore, the final cosmology constraints.

We have so far performed a number of tests that can probe the impact of inhomogeneity. For example, in PAPER I, we performed a series of null tests on the shear catalog and showed there are no residual systematics at the precision level of the catalog. In PAPER II, we showed that two independent methods of photometric redshift estimation — which will have different responses to inhomogeneous survey conditions — result in consistent $n(z)$ estimates. These are only implicit tests of the impact of inhomogeneity. In this paper, we perform an explicit, end-to-end test for the impact of inhomogeneity on our cosmology constraints. We describe below our methodology for this test.

6.1 Methodology

Our end-to-end test involves splitting the source-galaxy sample into subsets (usually halves) based on some criteria (see Section 6.2 and 6.3) and redoing all measurement and calibration steps; this includes the shear calibration (PAPER I), redshift estimation/calibration (PAPER II), analytical covariance generation, data vector measurements, and cosmological inference (this work). We consider splits both on the survey area and on the galaxy properties. The former is a clean split on the inhomogeneity in the survey image quality, whereas the latter can isolate subsets of the catalog that may be more susceptible to systematics of a specific kind. We briefly detail all the steps in the pipeline that are re-run for each subset:

Shear weights and response grid. PAPER I and PAPER II

detail the weights used in the different pieces of the cosmology analysis pipeline. In particular, we use shear weights (inverse-variance weights) and responses, both defined on grids of signal-to-noise and size. In our inhomogeneity tests here, these two grids are regenerated for the exact samples defined in each split. While it is fine to use the fiducial weights with no changes (this only risks performing a sub-optimal analysis but not a biased one) it is important to define the response grid consistently, as the object response is needed to make a robust estimate of the $n(z)$ for a given sample (MacCrann & Becker et al. 2022, PAPER II). For this reason, we remake the weight and response grids for each subset.

Shear Calibration. As described above in Section 3.3, all cosmology analyses of weak lensing require some calibration of the multiplicative bias, m . This is often done using image simulations of the survey, which is also the approach in DECADE as detailed in PAPER I. We use the existing, simulated catalog and repeat the estimates of m , while incorporating the new selection function (which defines the split) that is being applied to the data.

Redshift estimation. For our cosmology analysis, we estimate the $n(z)$ using Self-Organizing Maps (SOMs; Kohonen 1982; Kohonen 2001; Carrasco Kind & Brunner 2014; Masters et al. 2015) and the technique is denoted as SOMPZ (Buchs et al. 2019; Myles & Alarcon et al. 2021). One aspect of this method is classifying the source galaxies into a set of phenotypes, \hat{c} (see PAPER II). For these split tests, we do not reassign galaxies to a given phenotype and simply use the existing classification.⁶ However, we redo the selection of galaxies into four tomographic bins, and the estimation of the $n(z)$ per tomographic bin. This includes re-estimating the transfer function — through the BALROG synthetic source catalog built for DECADE — to connect the true properties of a galaxy with its observed properties. In all cases, we apply the same area/property selections to the galaxy samples. We generate a large number of $n(z)$ realizations, as is done in PAPER II, and characterize the uncertainty in the mean using the same method as described in that work. We do not repeat any measurements of the clustering redshifts; these measurements are only used as a cross-check in PAPER II and do not inform the fiducial $n(z)$ used in our analysis.

Covariance matrix. We estimate new n_{eff} and σ_e quantities (effective number density and shape noise of source galaxies) for the sample in our subset. We also recompute the geometry of the survey footprint, incorporating our new selections, and use it in conjunction with the new $n(z)$ to generate our analytic covariance matrix. This is done through CosmoCov, as is described above in Section 4.2.

⁶ This choice induces no bias in the derived $n(z)$ and only impacts their potential “optimality”; namely the overlap between the redshifts distributions of two tomographic bins.

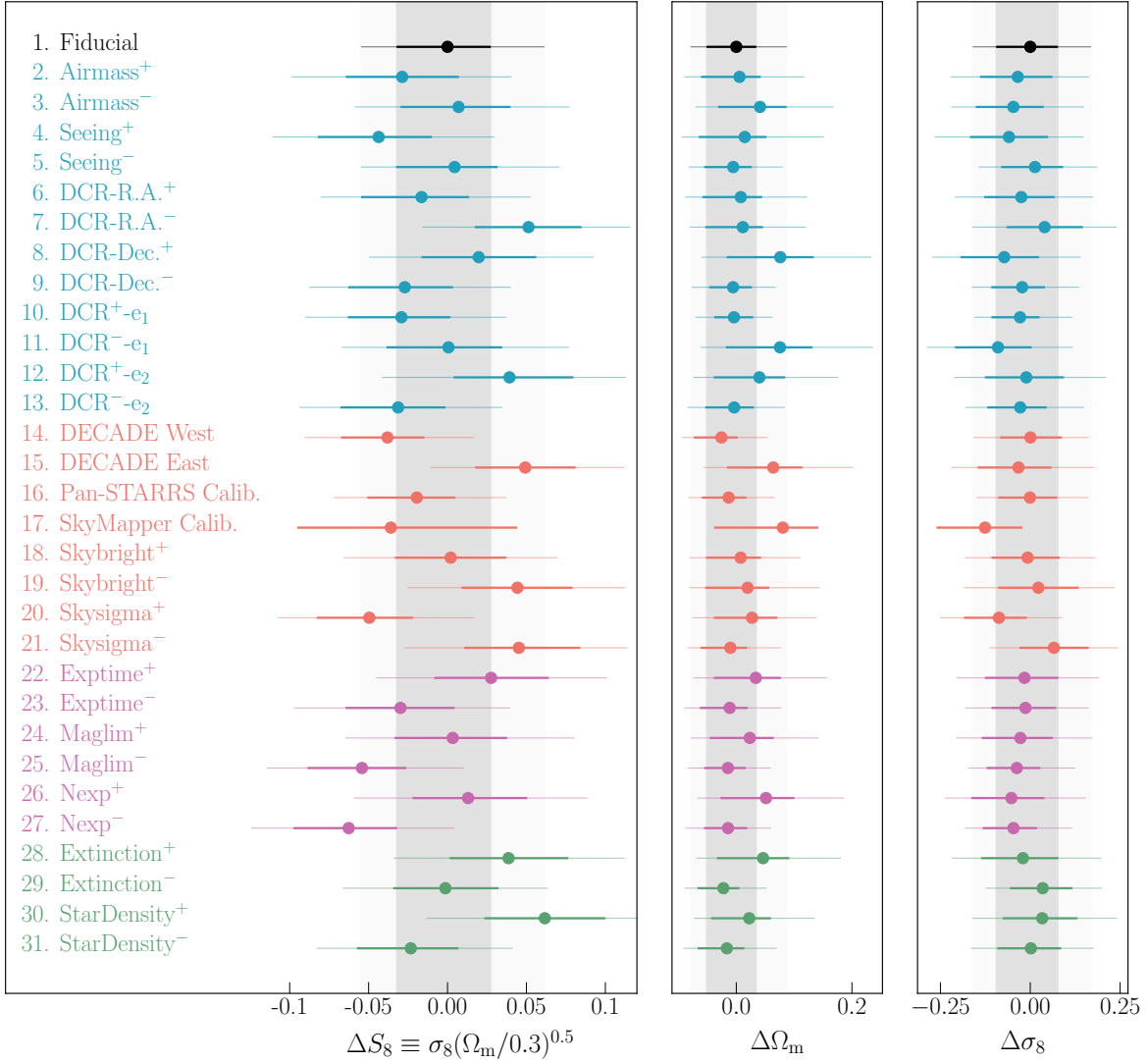


Figure 4. The constraints on S_8 from different subsets of the DECADE footprint, while consistently re-deriving all calibrations, redshift distributions, covariance matrices etc. The first, “Fiducial” constraint is using data the entire dataset. The rest, from top to bottom, split the survey based on: airmass, seeing (PSF width), DCR effects in celestial/ellipticity coordinates, the east/west regions, the Dec. ≥ -30 region where photometric calibrations used Pan-STARRS/SkyMapper, the sky background brightness and variations, exposure time, magnitude limit, number of exposures, interstellar extinction coefficients, and *Gaia* stellar number density. Analyses with X^+ (X^-) use the area with higher (lower) values than the median. The data vectors in each subset have essentially independent noise realizations and so the cosmology constraints can exhibit relative shifts of up to 3σ due to just statistical fluctuations. We show the parameter constraints relative to the fiducial estimate, with thick and thin horizontal lines denoting the 68% and 95% intervals for each constraint, respectively. For visibility reasons, we do not show the 95% interval for the “SkyMapper” subset alone. Most (all) deviations are within 1σ (2σ) of the fiducial results. The constraints from a subset and its complement are always within 2σ as well. No split exhibits shifts in cosmology that are larger than the expected variation from shape noise and cosmic variance. The footprints corresponding to the splits are shown in Figure A3.

Data vector and cosmology. We re-measure the data vector using only galaxies in the chosen part of the footprint, while using the new tomographic bin separations and the new shear weights. During our internal tests, the data vectors from this step were all blinded using the same random seed used on the data (PAPER IV). However, our results presented below are the constraints re-evaluated after unblinding the data vector.

Consistency. Finally, we must define a metric that allows

us to determine whether constraints from different subsets are consistent with each other and with the fiducial constraints. We do so using the standard score (or “Z-score”) for S_8 ,

$$\text{number of } \sigma = \frac{[S_8]_1 - [S_8]_2}{\sqrt{\sigma([S_8]_1)^2 + \sigma([S_8]_2)^2}}, \quad (11)$$

where $[S_8]_i$ and $\sigma([S_8]_i)$ are the mean and standard deviation of the posterior for constraint i . Unlike the previous tests, which involved consistency between analysis choices

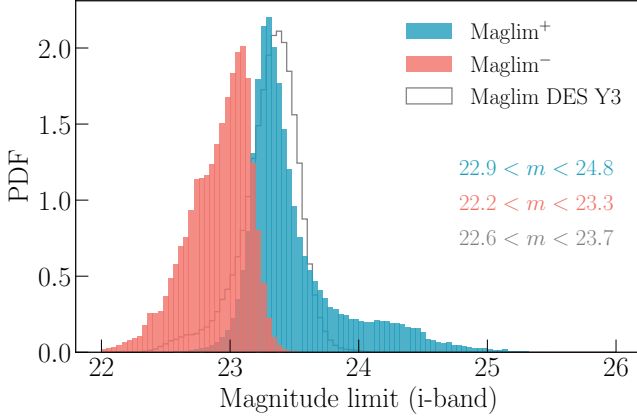


Figure 5. The distribution of magnitude limits in the i -band (from a HEALPIX map of NSIDE = 4096) for the two subsets of the DECADE footprint split by magnitude limit, and for the DES Y3 footprint. The Maglim⁺ region has twice the width of the other two samples. The ranges in the figure denote the 1% and 99% values of the distribution. There is a slight overlap in the two DECADE distributions as we plot values from the NSIDE = 4096 maps, whereas the selection mask is defined using the downgraded NSIDE = 1024 maps (see Section 6.2 for details).

operating on the exact same data vector, this test uses data vectors with different noise realizations that are essentially uncorrelated,⁷ since they access different subsets of galaxies from different subregions of the DECADE footprint. For this reason, it is possible for cosmology constraints from a given split to be different purely due to random fluctuations (where the fluctuations are dominated by shape noise, but will also have some cosmic variance component). Thus, our null test is satisfied if the S_8 constraints from a given subset are within 3σ of the constraints from the complementary subset. Though, in practice, we find all our consistency estimates are comfortably below this threshold. Here, we define complementary subset as “all galaxies not in the subset”.

In summary, we redefine the sample selection function to include a selection on survey area/object properties, and repeat all measurements that depend on the selection function. We then check if the cosmology constraints made using subsets of our data are statistically consistent with their complement, and also statistically consistent with the fiducial constraint corresponding to the entire DECADE dataset.

⁷ The shape-noise realizations are completely uncorrelated between two subsets that use different galaxies in their measurements. However, the cosmic shear measurements can still be correlated due to large-scale density fluctuations that are shared by subsets spanning adjacent regions of the sky. This is the “super sample covariance” discussed in Section 4.2. We note that shape noise is the dominant contributor to the measurement covariance.

6.2 Survey property splits & results

We first split on a number of different area-dependent quantities, most of which are informed by the survey observing conditions. In PAPER I (see their Figure 13), we check that the measured galaxy shapes are not correlated with a wide variety of survey properties: the seeing (PSF width), airmass, differential chromatic refraction (DCR) in e_1 and e_2 directions, DCR in the right ascension and declination directions, the magnitude limit, exposure time, number of exposures, the standard deviation of the sky background, and the sky brightness. We use this same set of maps in our test here, and also add a number of additional splits defined below. Every survey property map has four variants, for the $griz$ bands. The g -band data is not used in any of our lensing analysis. Of the remaining three, we choose the i -band maps for all our inhomogeneity tests.

We also split the footprint based on the *Gaia* stellar density (Gaia Collaboration 2021) and interstellar extinction maps from Schlegel et al. (1998), which were used in PAPER I to define our foreground mask (see discussion in Section 2.1). In all these cases, we split the footprint by sampling the map value for every object in our source-galaxy sample, finding the median value for the sample, and splitting the area of the sky based on that median. This ensures the splits contain an equal number of galaxies. The maps are downsampled to NSIDE = 4096 \rightarrow 1024 to improve the overall contiguousness of the selection mask by reducing the presence of disconnected islands. The remaining two split definitions are purely geometric (selections on R.A. and Dec. alone). First, we split our survey on Dec. ≥ -30 as all CCD images in regions north (south) of this line used the Pan-STARRS-1 (SkyMapper) measurements — as found in the ATLAS RefCat2 reference catalog (Tonry et al. 2018) — for their photometric calibrations (see Tan et al. 2024, for more details). Second, we split the footprint into an eastern and western footprint, split on R.A. ≥ 180 .⁸ In total, we define fifteen different criteria for splitting the footprint.

Figure 4 shows the results from all fifteen criteria, which corresponds to thirty different subsets of our footprint. The splits across survey properties often fill our full footprint in a somewhat patchy manner (see Figure A3), whereas the splits on geometry are distinct, internally contiguous footprints. In all cases, the data in the subsets will have independent realizations of the shape noise. The results in Figure 4 show that for any chosen subset, the constraints from the subset and its complement are within 2σ of each other. The blue set of points, which are all PSF-related, are correlated with each other, as are the purple set of points, which are all related to

⁸ We assign the entire SkyMapper-calibrated region (DEC. < -30) to the western footprint as both regions were part of the same, internal image processing run.

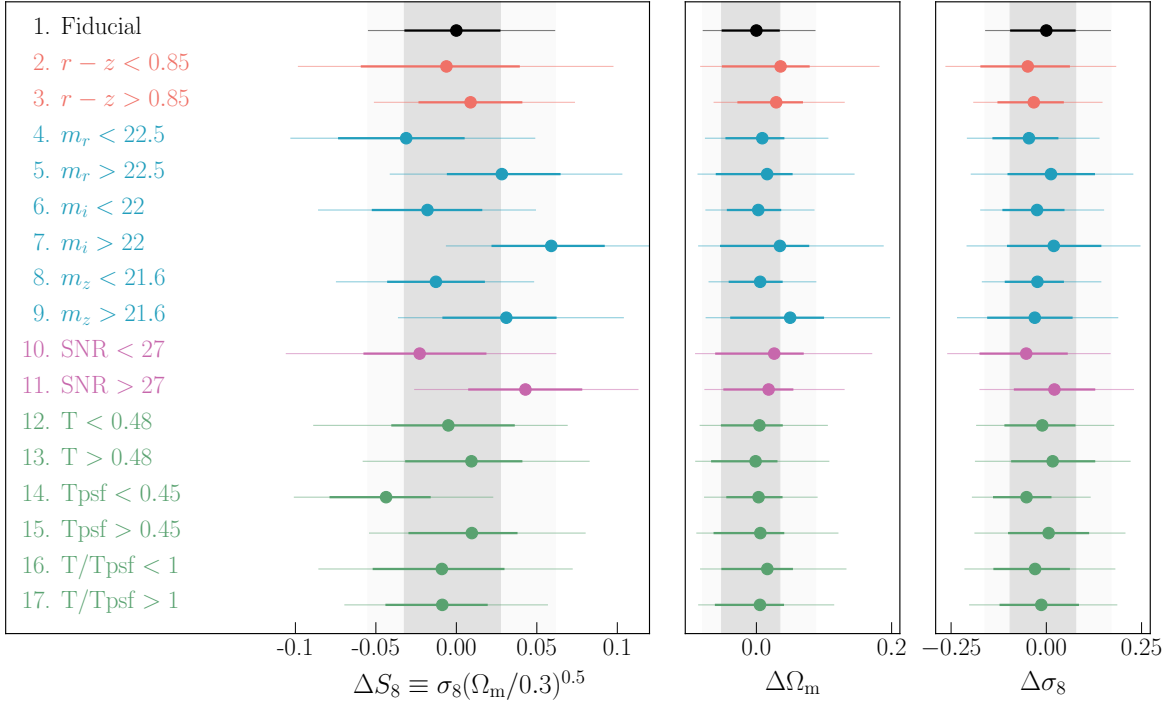


Figure 6. Similar to Figure 4 but now splitting the shear catalog on a variety of galaxy properties. From top to bottom, we split the catalog based on: $r - z$ color, magnitude in riz bands, signal-to-noise, the object size (in arcsec^2), the PSF size (in arcsec^2), and the ratio of object size to PSF size. All quantities are taken from the METACALIBRATION catalog.

image depth. In summary, we find that all thirty splits are within 2σ of the fiducial result, and each subset is within 2σ of its complement, which passes our 3σ criteria.

Area-dependent $n(z)$: While the above tests do not explicitly probe the impact of spatially correlated variations on the $n(z)$ estimates, they still implicitly check this effect. In particular, the regions of the sky with a higher magnitude limit are also regions with a significantly larger variation in the magnitude limit. Figure 5 shows distributions of these limits, and lists the 1% and 99% values of the distributions. The Maglim⁺ distribution is nearly twice as wide as the Maglim⁻ and DES Y3 distributions. Thus, any spatially varying $n(z)$ effects will be even more prominent in the Maglim⁺ region. The consistency of the cosmology from the Maglim⁺ and Maglim⁻ regions (the constraints are within 1.2σ as shown in Figure 4) suggests our final cosmology result is not significantly impacted by such area-dependent redshift effects.

6.3 Object property splits & results

We now repeat the analysis of Section 6.2 but splitting the sample on *galaxy properties* rather than through a survey mask. While this is not a strict test of spatial inhomogeneities, the property splits will isolate subsets of the catalog that may be more susceptible to inhomogeneity in various observing

conditions; for example, the shapes and photometry of galaxies with small sizes can be more strongly affected by PSF variations. All properties used in the splits are taken from the METACALIBRATION catalog, as this allows any selection-based bias in the shear to be robustly calibrated through the METACALIBRATION formalism (e.g., Sheldon & Huff 2017). We split on colors, magnitudes, signal-to-noise ratios, and sizes. The color split is motivated by Samuroff et al. (2019) and McCullough et al. (2024) who split the DES Y1 and Y3 sample, respectively, into red and blue galaxies and redo the cosmic shear analysis for each split. Their color split (see Table 1 in McCullough et al. (2024)) is a $r - z$ cut that *depends on the tomographic bin*. Given the setup of our pipeline, we only perform a non-tomographic $r - z$ split across the full catalog. We choose $r - z \geq 0.85$ as it is the median value, across the four bins, used in McCullough et al. (2024). We then consider a range of magnitude cuts and size cuts, which probe depth-based and PSF-based effects, respectively. The signal-to-noise cut is correlated with both magnitude and size-based cuts. All the non-color selections were defined using the median value of their distributions in the fiducial shape catalog and the chosen values are listed alongside our results.

Figure 6 shows the constraints from the different splits. Similar to the test in Section 6, most (all) constraints from the subsets are within 1σ (2σ) of the “Fiducial” estimate. Each subset and its complement, for all splits, are also consistent

within 2σ of each other. These results showcase the robustness of our cosmology results against systematics that preferentially affect certain types of objects in the catalog (*e.g.*, small objects) and further highlight that the cosmic shear analysis pipeline can handle data of a less pristine nature.

Other results associated with the above tests, such as the selection mask definition and the estimated redshift distributions, are presented in Appendix B.

7 SUMMARY

In this paper, we outline the methodology used to perform the cosmological inference of the Dark Energy Camera All Data Everywhere (DECADE) shear catalog. The modeling framework and implementation builds heavily on the DES Year 3 cosmic shear analysis (Secco & Samuroff et al. 2022; Amon et al. 2022), and incorporates recent updates as well (DES and KiDS Collaborations et al. 2023). After describing the basic modeling choices, we perform a series of specific tests to: (1) ensure that our baseline analysis choices are robust to different choices in the model, and; (2) stress-test our pipeline by performing the same analysis on forty-six different subsets of the dataset, each defined as a selection on observing conditions or galaxy properties. Some of these tests are particularly important as the DECADE dataset is a compilation of very different DECam observing campaigns and thus, the characteristics of this dataset are more inhomogeneous than conventional weak lensing surveys.

We summarize our main points below:

- Our fiducial model uses HMCode for the nonlinear matter power spectrum but does not marginalize over baryonic effects. Instead we remove the small-scale data points that can be contaminated from the presence of such baryonic effects. Our fiducial analysis uses similar scale cuts to the Fiducial DES Y3 analysis. We use the TATT intrinsic alignment model and a one-parameter shift (per tomographic bin) for the redshift uncertainty.
- For the covariance matrix, we use CosmoCov to generate an analytical covariance matrix that includes both Gaussian and non-Gaussian contributions. We also specifically test the shape noise model for the covariance matrix using simulations and find that the inhomogeneity in the galaxy distribution (at the level seen in DECADE) does not appreciably impact the model predictions.
- Our expected constraint power is similar to the DES Y3 “Fiducial” analysis constraints but 50% worse than the DES Y3 “Optimal” analysis constraints, given the latter removes significantly fewer scales in its analysis.

- We stress-test our methodology by rerunning the end-to-end pipeline, from catalog to cosmology, after splitting the DECADE catalog into subsets based on various observing conditions or measured galaxy properties. Overall, we tested twenty-three different definitions of the split (forty-six subsets in total). This test checks whether the spatially inhomogeneous nature of the subset can introduce significant biases (relative to the posterior width) in the cosmological constraints. Over the forty-six runs, the resulting cosmological constraints are mostly (always) within 1σ (2σ) of the fiducial constraints, indicating all subsets of the data show statistically consistent cosmological constraints.
- This is the first time the above end-to-end test is done with such completeness in a weak lensing survey. This was made possible by self-consistently recalibrating the shear estimates, remeasuring the redshift distributions and calibrations, re-deriving the covariance matrix estimate, and re-measuring the data vectors for each subset of the data. We find these tests cover a wide range of systematics in the catalog and recommend future surveys setup infrastructure to enable easy repetition of the processes in their end-to-end pipeline.

This work is part of a series of papers. PAPER I details the shear catalog and all associated systematic checks while PAPER II describes the redshift distribution and its associated validations/calibrations. The cosmological constraints from the DECADE data, derived using the full analysis methodology discussed here, are presented in PAPER IV.

Finally, we re-iterate the last point from our summary: there is significant value in building analysis frameworks that can easily ingest object selection functions defined by a user, and then use it in all steps of the end-to-end cosmic shear pipeline. In this work, we have discussed such functionality in the context of systematics validation, where it is a vital tool in checking that different subsets of the catalog produce statistically consistent cosmology constraints. However, we note that such functionality inherently increases the power and applicability of these datasets to the broader community. For example, combinations of lensing data with other datasets may benefit from using different galaxy selection functions, or different definitions for the tomographic bins. For example, additional selections on the source galaxies can improve the lensing-based mass estimate of galaxy clusters (*e.g.*, Rau et al. 2024), while cross-correlations with other surveys/datasets often use only a subset of the photometric survey (*e.g.*, Shin et al. 2019; Omori et al. 2023; Chang et al. 2023; Sánchez et al. 2023; Anbajagane et al. 2024b), and this can be done more robustly by re-calibrating the relevant subset of the data. Even in lensing-only analyses, we have

found uses for alternative tomographic binning of the data (Secco et al. 2022), and also for using different selection functions to isolate data that may be uniquely robust to certain systematics (Samuroff et al. 2019; McCullough et al. 2024). Building such functionality into our future pipelines will significantly improve the usability of lensing data, and enable the broader astrophysics and cosmology community to take better advantage of our precision datasets.

ACKNOWLEDGEMENTS

DA is supported by the National Science Foundation (NSF) Graduate Research Fellowship under Grant No. DGE 1746045. CC is supported by the Henry Luce Foundation and Department of Energy (DOE) grant DE-SC0021949. The DECADE project is supported by NSF AST-2108168 and AST-2108169. The DELVE Survey gratefully acknowledges support from Fermilab LDRD (L2019.011), the NASA *Fermi* Guest Investigator Program Cycle 9 (No. 91201), and the NSF (AST-2108168, AST-2108169, AST-2307126, AST-2407526, AST-2407527, AST-2407528). This work was completed in part with resources provided by the University of Chicago’s Research Computing Center. The project that gave rise to these results received the support of a fellowship from “la Caixa” Foundation (ID 100010434). The fellowship code is LCF/BQ/PI23/11970028. C.E.M.-V. is supported by the international Gemini Observatory, a program of NSF NOIRLab, which is managed by the Association of Universities for Research in Astronomy (AURA) under a cooperative agreement with the U.S. National Science Foundation, on behalf of the Gemini partnership of Argentina, Brazil, Canada, Chile, the Republic of Korea, and the United States of America.

Funding for the DES Projects has been provided by the U.S. Department of Energy, the U.S. National Science Foundation, the Ministry of Science and Education of Spain, the Science and Technology Facilities Council of the United Kingdom, the Higher Education Funding Council for England, the National Center for Supercomputing Applications at the University of Illinois at Urbana-Champaign, the Kavli Institute of Cosmological Physics at the University of Chicago, the Center for Cosmology and Astro-Particle Physics at the Ohio State University, the Mitchell Institute for Fundamental Physics and Astronomy at Texas A&M University, Financiadora de Estudos e Projetos, Fundação Carlos Chagas Filho de Amparo à Pesquisa do Estado do Rio de Janeiro, Conselho Nacional de Desenvolvimento Científico e Tecnológico and the Ministério da Ciência, Tecnologia e Inovação, the Deutsche Forschungsgemeinschaft and the Collaborating Institutions in the Dark Energy Survey.

The Collaborating Institutions are Argonne National Laboratory, the University of California at Santa Cruz,

the University of Cambridge, Centro de Investigaciones Energéticas, Medioambientales y Tecnológicas-Madrid, the University of Chicago, University College London, the DES-Brazil Consortium, the University of Edinburgh, the Eidgenössische Technische Hochschule (ETH) Zürich, Fermi National Accelerator Laboratory, the University of Illinois at Urbana-Champaign, the Institut de Ciències de l’Espai (IEEC/CSIC), the Institut de Física d’Altes Energies, Lawrence Berkeley National Laboratory, the Ludwig-Maximilians Universität München and the associated Excellence Cluster Universe, the University of Michigan, NSF’s NOIRLab, the University of Nottingham, The Ohio State University, the University of Pennsylvania, the University of Portsmouth, SLAC National Accelerator Laboratory, Stanford University, the University of Sussex, Texas A&M University, and the OzDES Membership Consortium.

The DES data management system is supported by the National Science Foundation under Grant Numbers AST-1138766 and AST-1536171. The DES participants from Spanish institutions are partially supported by MICINN under grants ESP2017-89838, PGC2018-094773, PGC2018-102021, SEV-2016-0588, SEV-2016-0597, and MDM-2015-0509, some of which include ERDF funds from the European Union. IFAE is partially funded by the CERCA program of the Generalitat de Catalunya. Research leading to these results has received funding from the European Research Council under the European Union’s Seventh Framework Program (FP7/2007-2013) including ERC grant agreements 240672, 291329, and 306478. We acknowledge support from the Brazilian Instituto Nacional de Ciência e Tecnologia (INCT) do e-Universo (CNPq grant 465376/2014-2).

Based in part on observations at Cerro Tololo Inter-American Observatory at NSF’s NOIRLab, which is managed by the Association of Universities for Research in Astronomy (AURA) under a cooperative agreement with the National Science Foundation.

This work has made use of data from the European Space Agency (ESA) mission *Gaia* (<https://www.cosmos.esa.int/gaia>), processed by the *Gaia* Data Processing and Analysis Consortium (DPAC, <https://www.cosmos.esa.int/web/gaia/dpac/consortium>). Funding for the DPAC has been provided by national institutions, in particular the institutions participating in the *Gaia* Multilateral Agreement.

This paper is based on data collected at the Subaru Telescope and retrieved from the HSC data archive system, which is operated by the Subaru Telescope and Astronomy Data Center (ADC) at NAOJ. Data analysis was in part carried out with the cooperation of Center for Computational Astrophysics (CfCA), NAOJ. We are honored and grateful for the opportunity of observing the Universe from Maunakea,

which has the cultural, historical and natural significance in Hawaii.

This manuscript has been authored by Fermi Forward Discovery Group, LLC under Contract No. 89243024CSC000002 with the U.S. Department of Energy, Office of Science, Office of High Energy Physics.

All analysis in this work was enabled greatly by the following software: PANDAS (McKinney 2011), NUMPY (Van der Walt et al. 2011), SCIPY (Virtanen et al. 2020), and MATPLOTLIB (Hunter 2007). We have also used the Astrophysics Data Service (ADS) and arXiv preprint repository extensively during this project and the writing of the paper.

DATA AVAILABILITY

All catalogs and derived data products (data vectors, redshift distributions, calibrations etc.) will be made public upon acceptance of the cosmology results.

REFERENCES

- Alonso D., et al. 2019, *MNRAS*, 484, 4127
- Amon A., Efstathiou G., 2022, *MNRAS*, 516, 5355
- Amon A., et al. 2022, *Phys. Rev. D*, 105, arXiv:2105.13543
- Anbajagane D., et al. 2020, *MNRAS*, 495, 686
- Anbajagane D., Evrard A. E., Farahi A., 2022a, *MNRAS*, 509, 3441
- Anbajagane D., et al. 2022b, *MNRAS*, 510, 2980
- Anbajagane D., Pandey S., Chang C., 2024a, *The Open Journal of Astrophysics*, 7, 108
- Anbajagane D., et al. 2024b, *MNRAS*, 527, 9378
- Anbajagane D., et al. 2024c, *J. Cosmology Astropart. Phys.*, 2024, 062
- Anbajagane D., et al. 2025c
- Anbajagane D., et al. 2025b
- Anbajagane D., et al. 2025a
- Aricò G., et al. 2021, *MNRAS*, 506, 4070
- Asgari M., et al. 2021, *A&A*, 645, A104
- Barreira A., Schmidt F., 2017a, *J. Cosmology Astropart. Phys.*, 2017, 053
- Barreira A., Schmidt F., 2017b, *J. Cosmology Astropart. Phys.*, 2017, 051
- Barreira A., Krause E., Schmidt F., 2018, *J. Cosmology Astropart. Phys.*, 2018, 015
- Bartelmann M., Schneider P., 2001, *Phys. Rep.*, 340, 291
- Bigwood L., et al. 2024, arXiv e-prints, p. arXiv:2404.06098
- Blazek J. A., et al. 2019, *Phys. Rev. D*, 100, 103506
- Bridle S., King L., 2007, *New Journal of Physics*, 9, 444
- Buchs R., et al. 2019, *MNRAS*, 489, 820
- Carrasco Kind M., Brunner R. J., 2014, *MNRAS*, 438, 3409
- Chang C., et al. 2023, *Phys. Rev. D*, 107, 023530
- Chisari N. E., et al. 2018, *MNRAS*, 480, 3962
- DES Collaboration 2022, *Phys. Rev. D*, 105, 023520
- DES and KiDS Collaborations et al. 2023, *The Open Journal of Astrophysics*, 6, 36
- Dalal R., et al. 2023, arXiv e-prints, p. arXiv:2304.00701
- Davis C., et al. 2017, arXiv e-prints, p. arXiv:1710.02517
- Euclid Collaboration: Knabenhans M., et al. 2019, *MNRAS*, 484, 5509
- Fang X., Krause E., Eifler T., 2020a, CosmoCov: Configuration space covariances for projected galaxy 2-point statistics, Astrophysics Source Code Library, record ascl:2006.005
- Fang X., Eifler T., Krause E., 2020b, *MNRAS*, 497, 2699
- Flaugher B., et al. 2015, *AJ*, 150, 150
- Friedrich O., et al. 2021, *MNRAS*, 508, 3125
- Gaia Collaboration 2021, *A&A*, 649, A1
- Gatti & Giannini et al. 2022, *MNRAS*, 510, 1223
- Gatti & Sheldon et al. 2021, *MNRAS*, 504, 4312
- Gatti & Vielzeuf et al. 2018, *MNRAS*, 477, 1664
- Gebhardt M., et al. 2023, arXiv e-prints, p. arXiv:2307.11832
- Goldstein S., et al. 2024, *Phys. Rev. D*, 110, 083516
- Grandis S., et al. 2024, *MNRAS*, 528, 4379
- Handley W. J., Hobson M. P., Lasenby A. N., 2015, *MNRAS*, 450, L61
- Heymans C., et al. 2006, *MNRAS*, 368, 1323
- Hirata C. M., Seljak U., 2004, *Phys. Rev. D*, 70, 063526
- Hunter J. D., 2007, *Computing in Science and Engineering*, 9, 90
- Huterer D., et al. 2006, *MNRAS*, 366, 101
- Jain B., Seljak U., 1997, *ApJ*, 484, 560
- Jarvis M., Bernstein G., Jain B., 2004, *MNRAS*, 352, 338
- Joachimi B., et al. 2011, *A&A*, 527, A26
- Kohonen T., 1982, *Biological Cybernetics*, 43, 59
- Kohonen T., 2001, *Self-Organizing Maps*
- Krause E., Eifler T., 2017, *MNRAS*, 470, 2100
- Krause E., Hirata C. M., 2010, *A&A*, 523, A28
- Krause E., et al. 2021, arXiv e-prints, p. arXiv:2105.13548
- Lange J. U., 2023, *MNRAS*, 525, 3181
- Lee E., et al. 2022, *MNRAS*, 517, 5303
- Lemos & Weaverdyck et al. 2023, *MNRAS*, 521, 1184
- Lesgourgues J., 2011, arXiv e-prints, p. arXiv:1104.2932
- Lewis A., Challinor A., Lasenby A., 2000, *ApJ*, 538, 473
- Lim S. H., et al. 2021, *MNRAS*, 504, 5131
- Limber D. N., 1953, *ApJ*, 117, 134
- Loverde M., Afshordi N., 2008, *Phys. Rev. D*, 78, 123506
- MacCrann & Becker et al. 2022, *MNRAS*, 509, 3371
- Masters D., et al. 2015, *ApJ*, 813, 53
- McCullough J., et al. 2024, arXiv e-prints, p. arXiv:2410.22272
- McKinney W., 2011, *Python for High Performance and Scientific Computing*, 14
- Mead A. J., et al. 2016, *MNRAS*, 459, 1468
- Mead A. J., et al. 2020, *A&A*, 641, A130
- Mead A. J., et al. 2021, *MNRAS*, 502, 1401
- Ménard B., et al. 2013, arXiv e-prints, p. arXiv:1303.4722
- Miyazaki S., et al. 2018, *PASJ*, 70, S1
- Myles & Alarcon et al. 2021, *MNRAS*, 505, 4249
- Newman J. A., 2008, *ApJ*, 684, 88
- Omori Y., et al. 2023, *Phys. Rev. D*, 107, 023529
- Rau M. M., et al. 2024, arXiv e-prints, p. arXiv:2406.11950
- Samuroff S., et al. 2019, *MNRAS*, 489, 5453
- Samuroff S., et al. 2023, *MNRAS*, 524, 2195
- Sánchez & Prat et al. 2022, *Phys. Rev. D*, 105, 083529
- Sánchez J., et al. 2023, *MNRAS*, 522, 3163
- Schaye J., et al. 2010, *MNRAS*, 402, 1536
- Schlegel D. J., Finkbeiner D. P., Davis M., 1998, *ApJ*, 500, 525
- Schmidt F., 2008, *Phys. Rev. D*, 78, 043002
- Schneider A., Teyssier R., 2015, *J. Cosmology Astropart. Phys.*, 2015, 049
- Schneider M., et al. 2006, *ApJ*, 651, 14
- Schneider A., et al. 2019, *J. Cosmology Astropart. Phys.*, 2019, 020

Bin	α	β	η
1	0.0025 ± 0.0070	1.6347 ± 0.1630	-0.8548 ± 2.2794
2	-0.0136 ± 0.0077	1.7490 ± 0.1890	-3.2707 ± 2.0824
3	-0.0058 ± 0.0100	1.6712 ± 0.1818	-2.8773 ± 2.9182
4	-0.0015 ± 0.0107	1.8128 ± 0.2270	0.8296 ± 3.0527

Table A1. The PSF coefficients per tomographic bin, as used in Equation (A4), computed using galaxies from only a given tomographic redshift bin. All measured coefficients are statistically consistent with expected values of $\alpha \lesssim 10^{-3}$ and $\beta, \eta \sim 1$. The method for computing the coefficients follow that describe in PAPER I (see their Section 4.5).

Secco & Samuroff et al. 2022, *Phys. Rev. D*, p. 023515

Secco L. F., et al. 2022, *Phys. Rev. D*, 105, 103537

Shao M., Anbajagane D., 2024, *The Open Journal of Astrophysics*, 7, 29

Shao M. J., Anbajagane D., Chang C., 2023, *MNRAS*, 523, 3258

Sheldon E. S., Huff E. M., 2017, *ApJ*, 841, 24

Shin T., et al. 2019, *MNRAS*, 487, 2900

Stiskalek R., et al. 2022, *MNRAS*, 514, 4026

Takahashi R., et al. 2012, *ApJ*, 761, 152

Tan C. Y., et al. 2024, submitted to AAS Journals

Tonry J. L., et al. 2018, *ApJ*, 867, 105

Troxel M. A., Ishak M., 2015, *Phys. Rep.*, 558, 1

Troxel M. A., et al. 2018, *MNRAS*, 479, 4998

Van der Walt S., Colbert S. C., Varoquaux G., 2011, *Computing in Science and Engineering*, 13, 22

Virtanen P., et al. 2020, *Nature Methods*, 17, 261

Vogelsberger M., et al. 2020, *Nature Reviews Physics*, 2, 42

Wagner C., et al. 2015, *J. Cosmology Astropart. Phys.*, 2015, 042

Yamamoto & Becker et al. 2025, arXiv e-prints, p. arXiv:2501.05665

Zuntz & Sheldon et al. 2018, *MNRAS*, 481, 1149

Zuntz J., et al. 2015, *Astronomy and Computing*, 12, 45

A IMPACT OF PSF CONTAMINATION AND B-MODES

A1 PSF contamination

We denote the *measured* two-component galaxy ellipticity in bin a , as e_a^{obs} . This ellipticity will have some contribution from untreated PSF contamination, $e_a^{\text{obs}} = e_a^{\text{true}} + \delta e_a^{\text{psf}}$. Now we can write the two-point correlation of the shapes as,

$$\begin{aligned}
 \langle e_a^{\text{obs}} e_a^{\text{obs}} \rangle &= \langle (e_a^{\text{true}} + \delta e_a^{\text{psf}})(e_a^{\text{true}} + \delta e_a^{\text{psf}}) \rangle \\
 &= \langle e_a^{\text{true}} e_a^{\text{true}} + 2e_a^{\text{true}} \delta e_a^{\text{psf}} + \delta e_a^{\text{psf}} \delta e_a^{\text{psf}} \rangle \\
 &= \langle e_a^{\text{true}} e_a^{\text{true}} \rangle + \langle \delta e_a^{\text{psf}} \delta e_a^{\text{psf}} \rangle \quad (\text{A1})
 \end{aligned}$$

where we follow previous shape measurement literature in assuming e^{true} does not correlate with e^{psf} , i.e., we assume $\langle e^{\text{true}} e^{\text{psf}} \rangle = 0$.

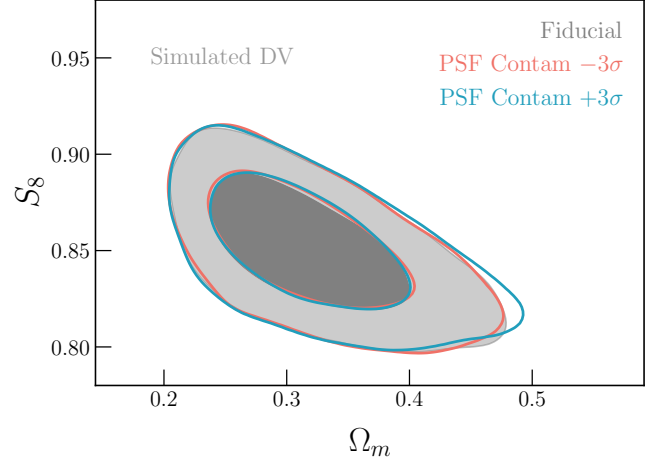


Figure A1. The impact of PSF contamination on the S_8 - Ω_m contours. We convert the distribution of α, β, η parameters (Equation A4) into additive offsets to the data vector, $\delta \xi_{\pm}^{\text{psf}}$, and contaminate a simulated data vector with the $\pm 3\sigma$ values of the $\delta \xi_{\pm}^{\text{psf}}$ distribution. The cosmology constraints are robust even after assuming extreme values of the PSF contamination.

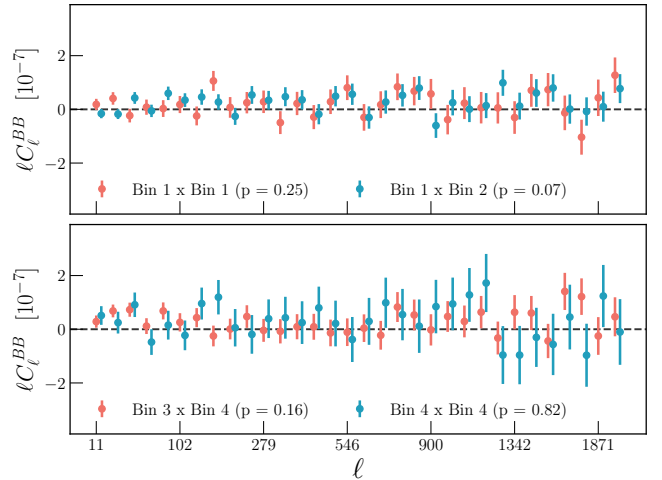


Figure A2. The angular power spectra of B -modes in the shape catalog, measured using galaxies from different tomographic bins (see legend). The measurements for all tomographic bin combinations are consistent with no B -mode signal. For brevity, we show only a subset of the measurements with the bin-combinations denoted in the legend.

Now, if we write the same for the cross-correlation,

$$\begin{aligned}
 \langle e_a^{\text{obs}} e_b^{\text{obs}} \rangle &= \langle (e_a^{\text{true}} + \delta e_a^{\text{psf}})(e_b^{\text{true}} + \delta e_b^{\text{psf}}) \rangle \\
 &= \langle e_a^{\text{true}} e_b^{\text{true}} + e_a^{\text{true}} \delta e_b^{\text{psf}} + \delta e_a^{\text{psf}} e_b^{\text{true}} + \delta e_a^{\text{psf}} \delta e_b^{\text{psf}} \rangle \\
 &= \langle e_a^{\text{true}} e_b^{\text{true}} \rangle + \langle \delta e_a^{\text{psf}} \delta e_b^{\text{psf}} \rangle \quad (\text{A2})
 \end{aligned}$$

for the same reasons mentioned above, e^{true} does not correlate with e^{psf} so the second and third term average to 0 given

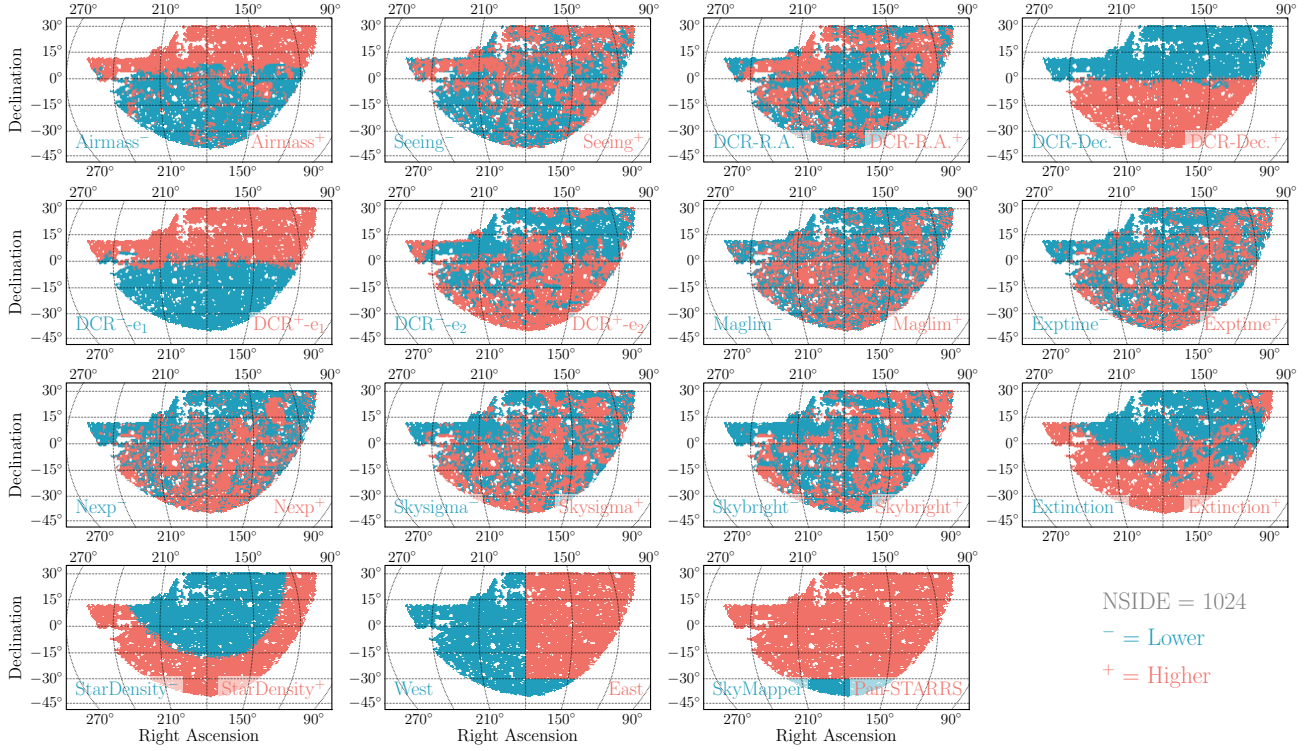


Figure A3. The area masks corresponding to each of the splits described in Section 6.2. We use the same \pm nomenclature to define regions where a given property is high/low. All survey property maps were generated at $\text{NSIDE} = 1024$. The western region (“West”) is not a strict split on longitude and includes some extra area that was part of the same, internal image processing campaign as the rest of the western patch.

$$\langle \mathbf{e}^{\text{true}} \rangle = 0.$$

The PSF contribution to the measured ellipticity can be written as,

$$\delta \mathbf{e}_a^{\text{psf}} = \alpha_a \mathbf{e}^{\text{model}} + \beta_a (\mathbf{e}^* - \mathbf{e}^{\text{model}}) + \eta_a \left(\mathbf{e}^* \frac{T^* - T^{\text{model}}}{T^*} \right) \quad (\text{A3})$$

where the coefficients $\alpha_a, \beta_a, \eta_a$ are measured using only the galaxies in tomographic bin a . The quantities $\mathbf{e}^{\text{model}}, \mathbf{e}^*$, etc. are not dependent on tomographic bin, but the coefficients associated with a given term *does* depend on the bin. We can write the cross-term, $\langle \delta \mathbf{e}_a^{\text{psf}} \delta \mathbf{e}_b^{\text{psf}} \rangle$ as,

$$\begin{aligned} \langle \delta \mathbf{e}_a^{\text{psf}} \delta \mathbf{e}_b^{\text{psf}} \rangle &= \alpha_a \alpha_b \rho_0 + \beta_a \beta_b \rho_1 + (\alpha_a \beta_b + \beta_a \alpha_b) \rho_2 \\ &\quad + \eta_a \eta_b \rho_3 + (\eta_a \beta_b + \beta_a \eta_b) \rho_4 \\ &\quad + (\eta_a \alpha_b + \alpha_a \eta_b) \rho_5 \end{aligned} \quad (\text{A4})$$

where the ρ_i are the Rowe statistics as described in PAPER I.

We compute these bin-dependent coefficients using the same techniques as PAPER I (see their Section 4.5) but now with only the source galaxies in tomographic bin a . The coefficient estimates are listed in Table A1, and are consistent with the non-tomographic case presented in PAPER I. We then compute the PSF contamination to the shear two-point data vector, $\delta \xi_{\pm}^{\text{psf}}$, using Equation (A4) and the coefficients of Table A1. For each bin, we generate a distribution of $\delta \xi_{\pm}^{\text{psf}}$ contributions.

This is done by sampling from the joint posterior of the α, β, η parameters in that bin, and generate a $\delta \xi_{\pm}^{\text{psf}}$ per sample. We then compute the 99.7% upper/lower bounds on $\delta \xi_{\pm}^{\text{psf}}$ and use those two estimates to contaminate the simulated data vector. The constraints from the contaminated data vectors are shown in Figure A1. The shifts in the cosmology are completely negligible, indicating that PSF contamination has negligible impact on the DECADE cosmology constraints.

A2 B-modes

In PAPER I, we verify that the DECADE shape catalog does not contain any B -mode signal to within the statistical precision of the data. We now repeat this exercise, but perform the measurement for different tomographic bin combinations. Here, we have used the NAMASTER (Alonso et al. 2019) package to measure the B -modes power spectra in our data.

Figure A2 shows the results. We find no evidence of B -modes in any tomographic bin combination. Given we have no detection of a B -mode contamination, we do not estimate a $\delta \xi_{\pm}^{\text{B-mode}}$ contribution and propagate the impact of a B -mode contaminant to cosmology. This follows the choices in Amon et al. (2022). Note that the harmonic-space estimator here differs from the real-space estimator used in PAPER I. The former was chosen for this test as our original

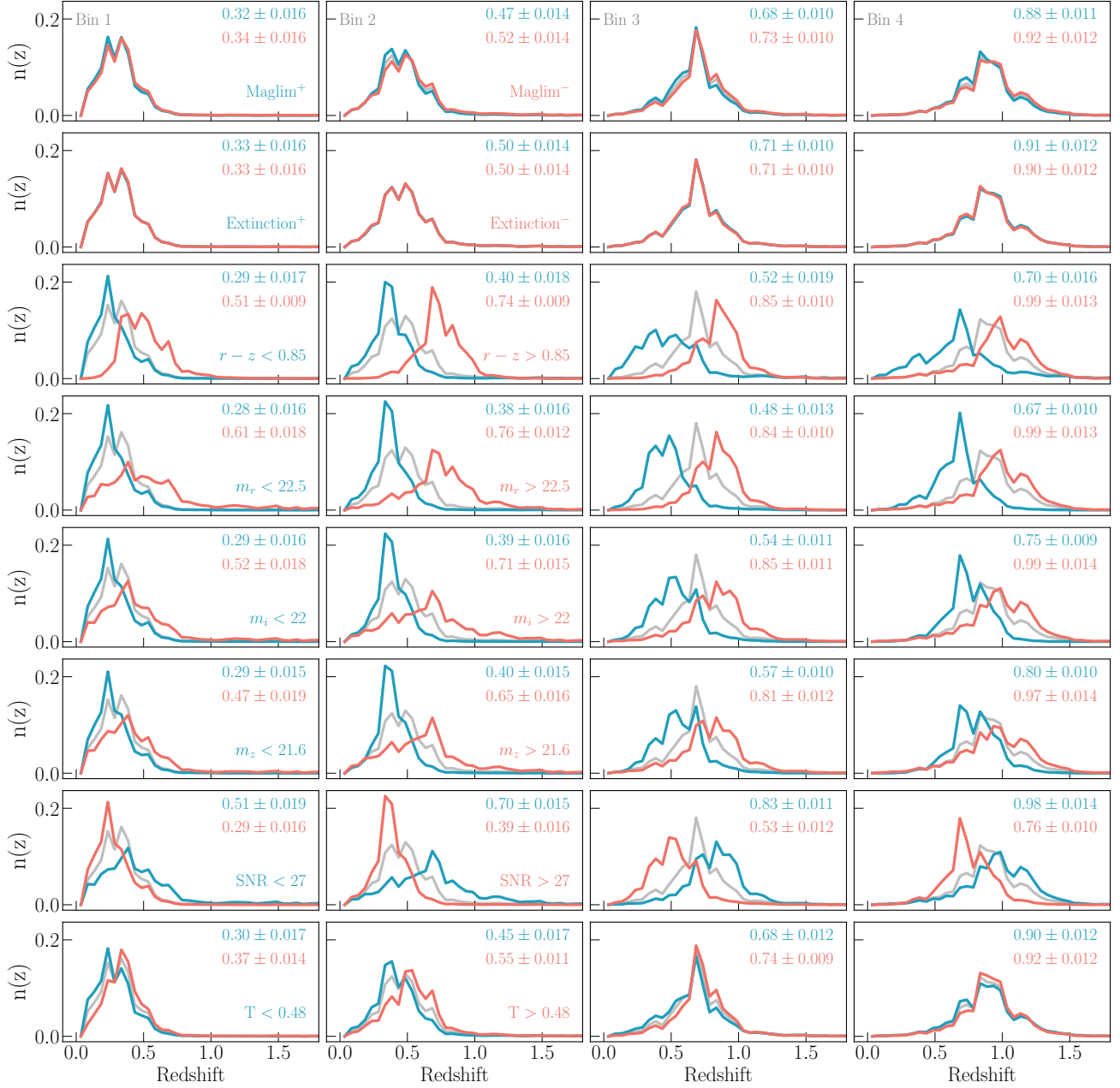


Figure A4. The mean redshift distributions for the four tomographic bins (columns) for some of the splits shown in Section 6.2 and 6.3. The fiducial redshift distribution is shown in gray. The text in the top shows the mean redshift, as well as the uncertainty on it as calibrated by the pipeline in PAPER II. The text also denotes the split corresponding to each color. The area-based splits only lead to minimal changes in the mean $n(z)$ — though they may have greater effects in causing spatially varying $n(z)$, which will not be highlighted in this figure which presents the area-averaged $n(z)$ — while the object-based splits cause a clear separation in redshift.

purpose was to contaminate the simulated data vector with B -modes (assuming a B -mode signal was detected) and this task requires as input the angular power spectra of B -modes. We have also verified that the non-tomographic measurement of the B -modes from NAMASTER is statistically consistent with no signal, which reproduces the result from the real-space estimator in PAPER I.

B ADDITION RESULTS FROM SURVEY PROPERTY SPLITS

Section 6.2 and 6.3 present cosmology constraints from different subsets of the footprint/catalog. Here, we denote some further details on the results in each split.

First, Figure A3 shows the footprint of the area-based splits used in Figure 4. The different colors distinguish the area

spanned by a given subset and its complement. The splits on airmass are highly correlated with those on DCR, while there are similar correlations between the splits on exposure time, exposure count, and magnitude limit, and also between the two Milky Way properties (star density and extinction). All maps are shown at $\text{NSIDE} = 1024$, which is the resolution used to make the splits.

Second, Figure A4 shows the redshift distributions of the tomographic bins for a handful of different split definitions. The gray line in all panels show the distribution from the “Fiducial” setup as a reference. The area-based splits lead to some visible (but still minor) modification to the overall $n(z)$. The object-based splits — which are done on object magnitudes or on quantities that correlate with object magnitudes — lead to a more significant shift in the redshift distributions. The text in each panel lists the mean redshift of each distribution, and the uncertainty on the mean for that subset, estimated using the full uncertainty-quantification procedure detailed in PAPER II.

C VALIDATION OF SHAPE NOISE TERM IN THE COVARIANCE MATRIX MODEL

As mentioned in Section 4.2, the \mathbf{C}_{SN} term includes the effect of the survey mask but not that of the variation in galaxy counts within said mask. However, we now show that the latter effect does not cause an appreciable shift in the covariance matrix estimates.

This validation is done by randomly rotating the measured ellipticities of the DECADE shape catalog and computing the ξ_{\pm} data vectors using TREECORR (Jarvis et al. 2004). Such techniques have been used, for example, by Troxel et al. (2018) for validating the shape noise model. By repeating this rotation step for $O(10^3)$ different realizations, we obtain a data-driven covariance matrix of ξ_{\pm} that includes only shape noise, but accounts for the relevant spatial variations in the data by directly using the positions and shapes from the DECADE

catalog. We also perform a variant where the data vector is computed after removing the inhomogeneities, simply by reassigning DECADE galaxies to new positions that now uniformly sample the survey mask. Figure C1 shows the ratio between the shape noise terms from the simulation-based method relative to those from the analytic method. This comparison is done for both the fiducial simulation-based covariance as well as the one with randomized galaxy positions; note that the analytic estimate is the same in either comparison. We find that in both cases, the analytic method matches the simulated one to within 5%. The fact that both sets of points are consistently within 5% of the analytic estimate highlights that the spatial variation of the galaxy number density is a negligible factor in calculating the \mathbf{C}_{SN} term. The errorbars on the simulation covariance matrices are estimated using a leave-one-out jackknife, *i.e.*, we remove one simulated data vector from the full set and generate the covariance matrix.

Finally, we have also compared the analytical covariance matrix (using all terms in Equation 7) with a jackknife-based covariance matrix computed on the data. The main additional aspect that this checks — beyond the test above — is any significant discrepancy in the off-diagonal terms of the covariance matrix. However, the relative differences of the two estimates depends on the cosmological parameters assumed for the analytic estimate and therefore cannot be a rigorous test before unblinding our cosmology constraints. In addition, the jackknife method is known to be biased on large scales where the variation across jackknife regions is not fully Gaussian; we have also verified this limitation via simulated data vectors. As such, we performed this comparison only as an approximate check and do not show the results here given the limitations in their interpretability.

This paper was built using the Open Journal of Astrophysics L^AT_EX template. The OJA is a journal which provides fast and easy peer review for new papers in the astro-ph section of the arXiv, making the reviewing process simpler for authors and referees alike. Learn more at <http://astro.theoj.org>.

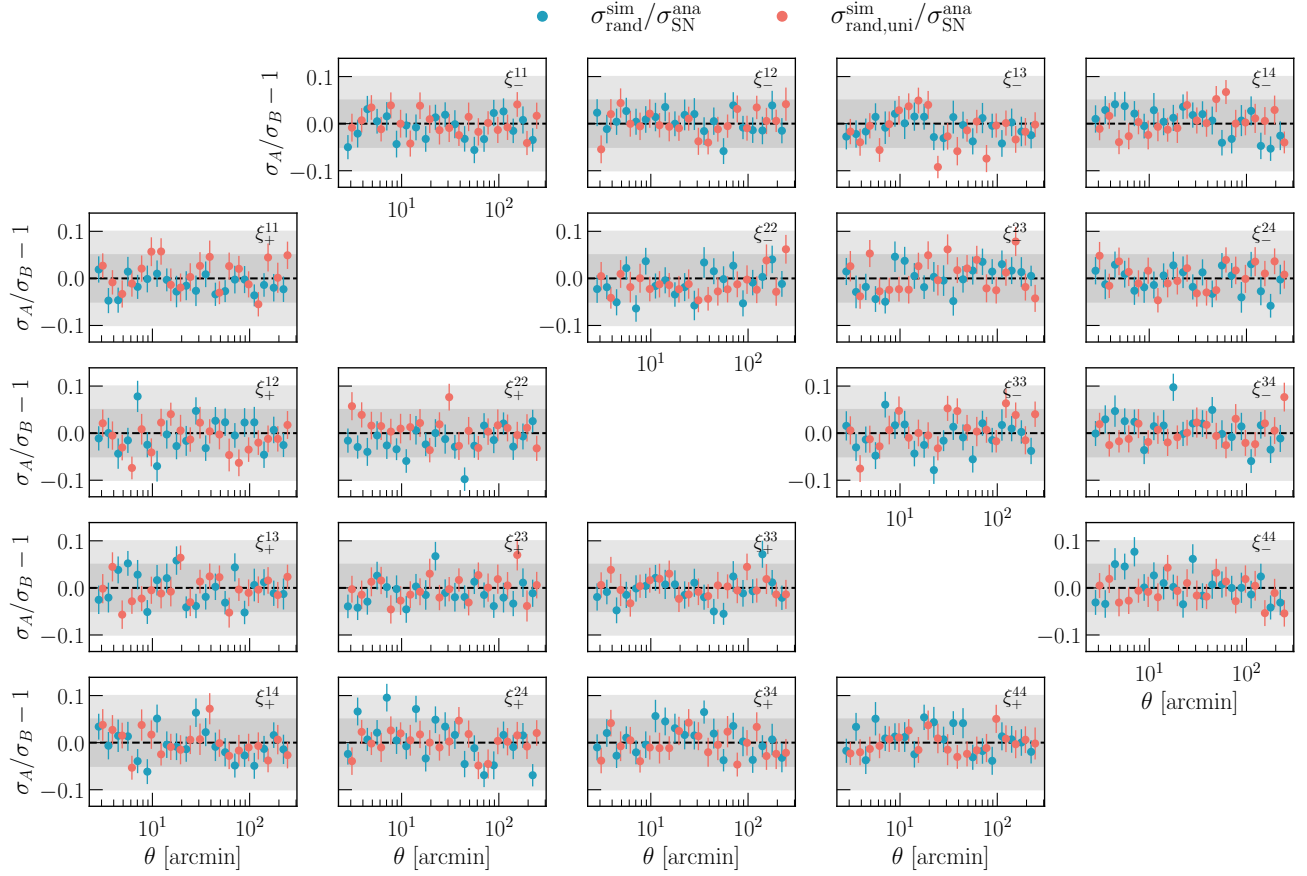


Figure C1. Ratios of the shape noise component in the covariance matrix between that measured from 600 simulations and analytical predictions ($\sigma_{\text{SN}}^{\text{ana}}$). We show the square root of the diagonal of the covariance matrix for each bin pair, and for two scenarios: (1) where we use the galaxy positions that are identical to the data and contain some level of spatial inhomogeneity (blue, $\sigma_{\text{rand}}^{\text{sim}}$) and (2) where we reposition each galaxy randomly inside the footprint to create a homogeneously distributed sample (red, $\sigma_{\text{rand,uni}}^{\text{sim}}$). Both sets of points scatter within 5%, indicating our analytical prescription of shape noise is accurate. We further find that the two sets of points do not show any qualitatively different behaviors, indicating the spatial inhomogeneity in the galaxy number counts does not affect the shape noise component of the covariance significantly. Uncertainties on the simulation covariance are obtained from a leave-one-out jackknife across the 600 simulations.